Advanced Development of a Smart Material Design, Modeling, and Selection Tool with an Emphasis on Liquid Crystal Elastomers

DISSERTATION

Presented in Partial Fulfillment of the Requirements for the Degree Doctor of Philosophy
in the Graduate School of The Ohio State University

By

Jung-Kyu Park, M.S

Graduate Program in Mechanical Engineering

The Ohio State University

2012

Dissertation Committee:

Prof. Gregory N. Washington, Advisor

Prof. Marcelo J. Dapino, Co-advisor

Prof. Carlos E. Castro

Prof. Mark E. Walter

Abstract

Smart materials have significantly varied properties and their various types are used broadly in many different engineering applications. In order to grow the field and promote its long term viability, it is important to develop tools which enable researchers and practitioners to determine the best smart material for the application. Computerized material selection databases and systems have been recently developed by design and materials engineers to help users select the best materials for an application. However, documentation of smart materials is limited, especially for those aimed at the use of these materials in devices and applications.

In this dissertation, system-level simulation models and collected material data are compiled in a GUI-based computer software called Polymers and Smart Materials Software (PSMS). This material selection tool encompasses material properties and material-level models as well as systems level smart material applications for a wide range of smart materials. This type of compiled data can expedite the material selection process when designing smart material based systems by allowing one to choose the most effective material for the application. The PSMS tool consists of the following three major sections: 1) Polymers (Polymer types and properties, Polymeric behaviors including dielectric and liquid crystal elastomers); 2) Smart Materials (Piezoelectric Ceramics/Polymers, Shape Memory Alloys/Polymers, Thermoelectrics,

Electrorheological and Magnetorheological Fluids); 3) More information (External databases, Cost information, etc.).

The software tool offers a wide variety of design and selection features. Material property and performance charts are provided to compare material properties and to choose the best material for optimal performance. The tool is also flexible in that it enables users to categorize material properties and create their own databases. In areas where existing models were inadequate for systems level integration, new models were developed. Towards that end this dissertation highlights the modeling strategies being conducted in the area of liquid crystal elastomers.

The effectiveness and accuracy of the smart material selection tool are evaluated by comparing program outputs with other published experimental results from smart materials and devices. Based on the results, the material and device models are improved. The experimental verification of the material models is presented to show the reliable performance of the smart material design, modeling, and selection tool.

Dedicated to my grandmother, parents,

sisters, my fiancée Sanghee, and my mother-in-law-to-be

for their love, support and prayers

Acknowledgments

I would like to express my deepest appreciation towards my adviser, Prof. Gregory Washington for his academic guidance, patience, care and continuous support all through my graduate studies and research at The Ohio State University (OSU). I would also like to thank Prof. Marcelo Dapino, Prof. Carlos Castro, and Prof. Mark Walter for serving on my dissertation committee. I am thankful to Prof. Stephen Bechtel for taking time out to participate in my candidacy exam.

I am grateful to the member organizations of the Smart Vehicle Concepts Center and the National Science Foundation Industry/University Cooperative Research Centers program for supporting this work. I would like to extend my gratitude to Dr. Leon Headings for conversations related to research and other aspects of life. I am also grateful to other fellow graduate students in the Intelligent Structures and Systems Laboratory (ISSL), Dr. Prashanth Ramesh, Kyle Van Volkinburg, and Matt Detrick for their assistance and friendship during my work. I also thank Dr. Byeongil Kim, Dr. Younkoo Jeong, and Prof. Hwan-Sik Yoon who have helped and encouraged me throughout my life at OSU.

Finally, I would like to thank my grandmother, parents, sisters, mother-in-law-to-be, and brother-in-law-to-be for all of their continuous love, support, prayers. Especially, I would like to thank my fiancée, Sanghee Ryu for her faith and encouragement, while we have engaged in our doctoral studies together at OSU.

Vita

December 6, 1977 ....Born in Daegu, South Korea

February, 2000 ....B.S. Automotive Engineering and
Mechatronics Engineering,
Catholic University of Daegu, South Korea

June, 2004 ....M.S. Mechanical Engineering,
The Ohio State University, Columbus, OH

June, 2005 – August, 2008............................Associate Research Engineer,
Ssangyong Motors, South Korea

September, 2008 – present ....Graduate Research Associate,
Mechanical Engineering
The Ohio State University, Columbus, OH

Publications

J. Park, L.M. Headings, M.J. Dapino, J.W. Baur, and G.P. Tandon. Analysis of shape memory polymer-alloy composites: modeling and parametric studies. *ASME Conference Proceedings*, 8257, 2012.

J. Park and G. Washington. Advanced development of a smart material design modeling, analysis and selection software. *Journal of Intelligent Material Systems and Structures* (*submitted for publication*), 2012.

J. Park and G. Washington. Advanced development of a smart material design, modeling, and selection tool. *ASME Conference Proceedings*, 1(5217):675–684, 2011.

J. Park and G. Washington. Smart material database compilation and material selection tool development. *SPIE Conference Proceedings*, 7645-21, 2010.

J. Park, G. Washington, and H.-S. Yoon. A hybrid approach to model hysteretic behavior of PZT stack actuators. *Journal of Intelligent Material Systems and Structures*, 20(4):467–480, 2009.

Fields of Study

Major Field: Mechanical Engineering

Table of Contents

List of Tables

List of Figures

xiii

Chapter 1 : Introduction

1.1 Introduction and Problem Statement

Smart materials and elastomers have been broadly implemented in a variety of industries that include automotive, aerospace, military, biomedical, energy, electronics and chemical. General types of smart materials include piezoelectric, magnetostrictive, thermoelectric, magneto-rheological, electro-rheological, photomechanical, and shape memory materials. Although a significant amount of smart materials are being widely used in various engineering applications, there exists limited information on how to effectively use these materials, particularly when classes of these material are compared against one another. Moreover, documentation in general is scarce, outdated, lacks a connection to mathematical models and doesn't reflect recent advancements in the development of smart materials.

In this situation, it is important to produce a framework which is flexible enough to provide state-of-the-art information and can grow based on changes in the state-of-the-art. In addition, since the range of smart materials available to engineers and the demand of smart materials have continually increased, choosing the best material for optimal performance has become an important issue. In order to determine the best material for the application, key properties must be highlighted in the same context. Finally, modern analysis tools must incorporate material and systems cost if one is to develop a tool that will be used by practicing engineers.

In this research, a smart material selection tool was developed and incorporated into a software driven by Graphical User Interface (GUI) using Visual Basic™ and database software. The tool interface was designed specifically for modeling and performance based usage. This material selection tool encompasses material properties and material-level models as well as potential smart material applications. The tool allows users to categorize material properties and to create their own databases as well as to edit them. Ultimately, the compilation of a comprehensive database on smart materials will enable one to expedite the material selection process in the design of smart material devices or systems. Using this framework, smart material selection and system simulations and their corresponding industrial application designs can be improved in a time-efficient and cost-effective manner.

The primary goals of this research are: (1) to develop a GUI-based computer software that determines and simulates which smart material to use based on properties and performance, and (2) to develop effective models of smart materials which don't exist or are not suitable to be incorporated into a general input-output systems paradigm. Towards that end models are utilized for the primary smart material types (piezoelectric, thermoelectric, magnetorheological, electrorheological, and shape memory materials) and new models are developed for light-induced liquid crystal elastomers.

1.2 Motivation and Significance

Current databases for material selection have been developed by design and materials engineers. Database tools can assist designers in the selection of materials for manufacturing processes. The databases contain materials such as metals, polymers,

2

ceramics, glasses, and composites. Table 1.1 shows some databases for materials selection and the types of materials they contain.

Database \ Material	Metals	Polymers	Ceramics	Glass	Composites	Smart Materials
Granta Design	×	×	×	×	×	
Material ConneXion	×	×	×	×	×	
MatWeb	×	×	×	×	×	×
IdeMat	×	×	×	×	×	
Azo Materials	×	×	×		×	×
ASM Materials Information	×	×	×		×	
PolyInfo	×	×				

Table 1.1. Databases for Materials Selection

Question \ Database	Granta Design	MatWeb	IdeMat	Azo Materials	PSMS
Do they show information on material properties?	Yes	Yes	Yes	Yes	Yes
Do they provide analytical equations?	No	No	No	No	Yes
Do they have basic design equations?	Yes	No	No	No	Yes
Do they highlight smart materials?	No	Yes	No	Yes	Yes

Table 1.2. Databases and Questions

All current databases provide information on material properties, but they do not use analytical equations. The Granta Design only has basic design equations. MatWeb and Azo Materials highlight some smart materials. However, in these two databases,

3

documentation of smart materials is limited and does not relate the material directly to actuator and sensor design. No current databases incorporate modeling equations and provide a platform for incorporating advances in the state-of-the-art. Changes in the state-of-the-art cannot be overlooked as new or improved smart materials and devices are being introduced at a rapid pace. The new PSMS will therefore feature smart materials, provide modeling equations for actuator and sensor design, and allow for readily updated and customized databases.

According to a report published by BCC research (2011), the worldwide market for smart materials was estimated at $8.1 billion in 2005 and $19.6 billion in 2010 [1]. They now expect the market to exceed $22 billion in 2011 and to grow to $40 billion by 2016 (see Figure 1.1).
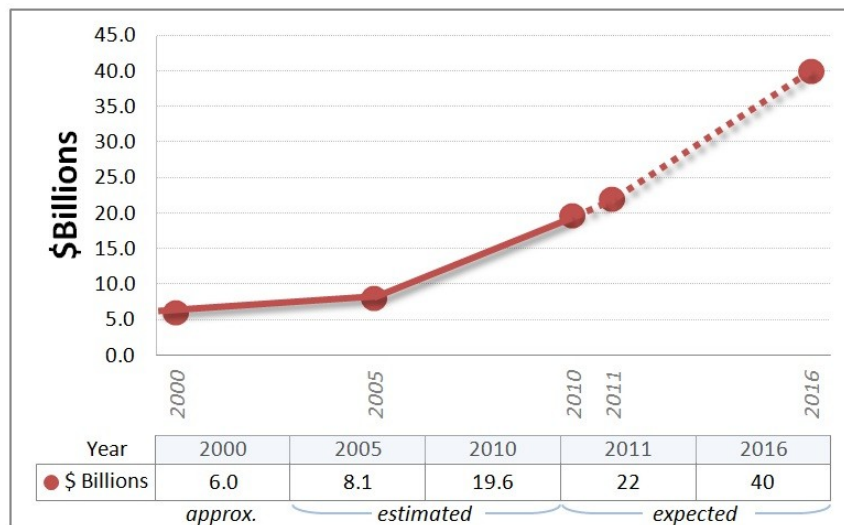
Figure 1.1. Global Market for Smart Materials (Data from BCC research [1])

The development of new materials and the demand for existing smart materials has continued to increase at an astounding pace. The range of smart materials and systems incorporating them available to engineers is much broader than just five years ago. It is now even more important to select the best material in an early design stage for low cost and better performing final products.

One limiting factor in this future growth is the availability of analysis tools, as contemporary engineering depends on these tools to develop the next generation of products. Comprehensive software analysis tools are needed to promote and accelerate future growth since most engineers are not familiar with these materials. Additionally, analysis tools help in the understanding of not only when, but how to use these materials as the nonlinearity of many of these materials, in certain operating regimes, limit their utility. For these reasons, the development of these software tools represents a significant advancement in the field.

1.3 Literature Review

The literature review conducted for this research is categorized into two different sections; 1) existing material selection databases and 2) modeling of smart materials. Section 2 contains an extended survey of literature on light-induced deformation of liquid crystal elastomers (LCE) since new LCE models were developed in this research.

1.3.1 Existing material selection databases

The significance of the knowledge of the diverse materials and their properties has increased more than ever before due to the broadening choices of the materials in recent years. As one of the responses to this need for knowledge, several material databases have been developed [2, 4]. In addition, computerized material selection databases and systems have been developed by design and materials engineers to help users select the best materials for a given application [4-7]. Materials selection plays an important role across a myriad of fields and for specific applications such as health monitoring of composite structures and manufacturing of micro-electro-mechanical systems [7, 8]. In this section, representative databases for material selection are introduced.

Matweb is the most comprehensive online database of properties in terms of the number of materials included in the databases [2]. At the present time, this database enables the users to search more than 90,000 materials and their properties [3]. The information provided includes categories such as physical, mechanical, thermal, optical, and electrical properties [2]. Although Matweb includes smart materials, the information has a limitation in that it does not provide modeling or expected performances

Granta Design, which includes material data and software tools, arose out of a collaboration between two engineering professors at the Cambridge University Engineering Department [9]. Professors Ashby and Cebon developed *Materials Selection Charts*, which display material property data and *performance indices* which are combinations of material properties related to performance [7]. They implemented these features in software called the Cambridge Materials Selector (CMS). An important

feature of the Granta Design is that its dataseries and modules contain a large number of materials both individually and in combination.

Material ConneXion is an online database which has opened new ways of material selection [2]. It was founded in 1997 by George M. Beylerian in an attempt to provide more dynamic ways to search for materials [10]. It provides easier ways to use the interface by providing good indicators and selection possibilities for uses [2]. It started with around 200 materials, but over a decade later, it contains thousands of materials [10]. However, it does not include smart materials.

As we discussed and highlighted in Table 1.1 and Table 1.2, these databases, while effective, do not include modeling equations, have very limited smart materials information, and are not easily reactive to changes in the state-of-the-art. For example, there are new classes of piezoelectric materials being developed which are wide bandgap semiconductors [11]. These databases lack a sufficient platform to incorporate these materials.

1.3.2 Modeling of smart materials

Dielectric Elastomers: Dielectric elastomers (DEs) are smart materials, which transform electrical energy (voltage) directly into mechanical energy (strain) and belong to a category of electroactive polymers (EAPs) [12]. Dielectric elastomer actuators have been shown to provide larger strains than other types of EAPs, higher energy density, considerable efficiency and fast response time [13, 14]. They are made up of two compliant electrodes and a thin elastomer film in between them [14]. A voltage applied to

7

the electrodes induces the deformation of the elastomer's film. An electric force causes the film to contract along the electric field direction. Due to the contraction, the elastomer film elongates in the direction of the film plane [14]. The motion or force generated by the in-plane strain is exploited for the applications of artificial muscles [15].

Several models for dielectric elastomers have been proposed [13, 16]. The Mooney-Rivlin model fits better than Hooke and Neo-Hookean models, but it doesn't accurately represent the strain-hardening region of a stress-strain curve which is present in rubberlike solids [17, 18]. Only the model introduced by Ogden fits the whole region including the strain-hardening [17]. Through the strain hardening process, the rubberlike solid becomes stronger and requires more force to be stretched. The Ogden model [19] describes a wide range of strain hardening and the constitutive behavior of a rubberlike solid. Several strain-energy functions have been introduced to model the strain hardening effect [20]. The stress-strain relation is obtained through evaluation of the strain-energy function. The Ogden model uses the strain energy function, which consists of principal stretch ratios, a strain hardening exponent and the interpretation of the shear modulus under infinitesimal straining [21].

Piezoelectric Ceramics and Polymers: Piezoelectric materials come in the form of a ceramic or a polymer. The most widely used piezoceramics are lead zirconate titanate (PZT). These materials are usually formed into a stack configuration or a thin wafer, and produce strain or mechanical deformation in response to an applied voltage (converse piezoelectric effect). They also produce a charge when they encounter an applied stress (direct piezoelectric effect).

A piezoelectric bimorph actuator consists of two thin piezoelectric ceramic layers and a thin passive metal plate in between them. They are bonded with the metal plate using an adhesive epoxy resin [22] and the polarization directions of the two PZTs, which can be switched, determine bimorph response.
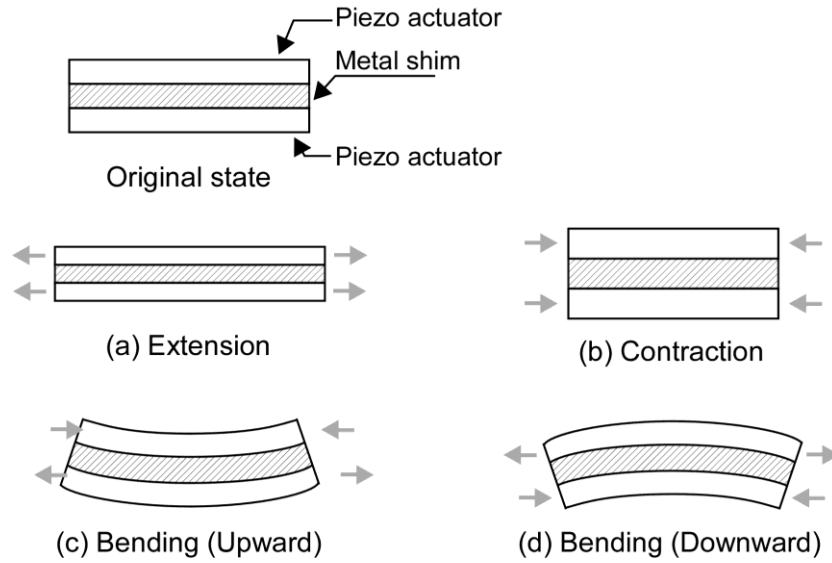
Figure 1.2. Piezoelectric Bimorph Deformation

When voltages are applied to oppositely poled PZT layers, one of the layers extends and the other one contracts. The induced bending moment causes the actuator to either bend up or down based on the polarity of the applied voltage. When the poling directions of the PZT layers are the same, the bimorph actuator only extends or contracts without causing any bending movements. A patch actuator consists of one or more layers of thin piezoelectric sheets [23]. Depending on the input type, it functions in either an actuation mode or a sensor mode. A tubular actuator is a hollow piezoceramic stack actuator with

electrodes on both the inside and outside diameters [24]. A multilayer stack actuator consists of stacked PZT wafers [25].

Rainbow/Thunder actuators are composed of one thin piezoelectric ceramic layer between a thin metal substrate and an electrode. RAINBOW stands for Reduced And INternally Biased Oxide Wafer [26]. THUNDER stands for THin layer UNimorph DrivER [27]. This type of actuator is called a unimorph and operated in a similar way to the bimorph. The deflection model of a bimorph given by Anderson [28] is modified for the unimorph case of the beam.

Polyvinylidene fluoride (PVDF) is a polymer piezoelectric film with strong piezoelectric and pyroelectric effects [29]. The electrode covering the film can be etched to assume multiple patterns lending themselves to multiple customized properties [30]. As an actuator, PVDF film conforms to the direct and converse piezoelectric effect as the material is piezoelectric. For high Q (low damping) structures, the induced bending caused by an actuator attached to a structure can reduce resonant vibrations of a flexible structure [31]. However, PVDF produces less actuation power than a piezoceramic provides due to its low stiffness [32]. As a sensor, the opposite is true as the electrodes act as detection sensors picking up the charge generated from the PVDF film. The film provides higher voltage output in response to an external pressure than PZT and a relatively wide bandwidth (up to 100MHz) [33]. Its high flexibility enables the thin piezoelectric film to be glued to virtually any surface [34].

Shape Memory Alloys: Shape memory alloys (SMA) are alloys that possess the ability to undergo significant shape deformation at low temperatures and retain this deformation until they are heated and their temperature exceeds their transition start

temperature [35]. This shape change known as the "shape memory effect" occurs as a result of a change in the atomic crystal structure of the alloy [36]. The well-known mathematical models are the Tanaka, Liang & Rogers, and Brinson models. The Tanaka model describes the thermomechanical constitutive equations and the transformation kinetics [37]. The Liang & Rogers model describes a unified thermo-mechanical constitutive law based on the Tanaka model. This model utilizes the same constitutive relationship that Tanaka used. The main difference arises in the development of the martensite volume fraction using the cosine function [38]. The Brinson model is derived based on the principles from the Tanaka model and the Liang & Rogers model. This model exhibits the desired characteristics such as critical stresses. The critical stresses at the start and end of the transformation are defined by the transformation equations of the Liang & Rogers model. In the Brinson model, the martensite volume fraction uses a modified cosine model and is divided into two parts such as applied stress part and temperature induced part [39].

Shape memory polymers: Thermally induced shape memory polymers (SMPs) are polymeric smart materials which can undergo deformation when heated above a glass transition temperature T_g and recover from a deformed shape to their memorized original shape when cooled. At temperatures below T_g, an SMP is in a glass phase and becomes sufficiently rigid to resist deformation. Conversely, an SMP is in a rubber phase above T_g and becomes highly deformable, exhibiting a large decrease in its Young's modulus. SMPs have several advantages over SMAs: they have a much lower density showing large strain recoverability up to 400%, a cheaper manufacturing cost, and are less massive [40]. Due to these characteristics, SMPs have been researched as promising

11

materials for morphing aircraft skins [41, 42]. On the other hand, SMPs generate lower actuation and recovery forces due to their material properties. In order to improve these mechanical properties, SMP composites with reinforcing fillers have been investigated [40, 43].

Thermoelectrics: A thermoelectric couple is a semiconductor couple with N- and P-type elements. A thermoelectric module consists of a set of thermoelectric couples configured thermally in parallel and electrically in series [44]. A temperature difference applied between the top and bottom sides of the thermoelectric module causes heat flow through the thermoelectric couples and induces voltage generation [45]. Thus, thermoelectrics can operate as power generators. Thermoelectrics can be used also as heat pumps, with an applied voltage causing heat to be absorbed at one side and expelled at the other. The heat pump can operate in either cooling or heating mode, depending on the polarity of the applied voltage.

Electrorheological and Magnetorheological fluids: Electrorheological (ER) fluids are suspensions containing dielectric micron-sized particles suspended in a non-conducting viscous carrier fluid. Magnetorheological (MR) fluids contain micron sized magnetic (ferrous) particles suspended within a carrier oil. In the presence of a magnetic field, the magnetic particles are polarized and form linear chains parallel to the applied field. The particle chain formation restricts the movement of the fluid, increasing the shear stress in the fluid. The change in shear stress is associated with particle density, particle size, carrier property, applied field, and other factors [46]. In the absence of an applied field, the rheological property of MR fluids is restored and the fluid flows more

freely. Thus the shear stress of the fluid can be controlled by varying the applied field. The controllable fluids have been employed for commercial applications [47].

1.3.3 Light-induced deformation of liquid crystal elastomers

Liquid crystal elastomers (LCEs) are composed of cross-linked liquid crystalline polymers exhibiting elastomeric properties. LCEs exhibit large bending and linear deformability under various stimuli such as heat, electricity, and light illumination. Especially, light as an external stimulus is employed to actuate LCEs because of its controllability in remote, rapid, and precise ways [48]. The large light-induced deformation in certain photochromic LCEs was reported in 2001 [49]. The photo-strain occurs due to the isomerization of azobenzene, which is the transition from the *trans*-state to the *cis*-state with absorption of the UV light. The photo-responsive LCEs have been researched for potential applications such as artificial muscles [50, 51] and actuators [52, 53].

Researchers have developed models of light-induced bending to understand the photo-responsive mechanism of LCEs. Warner and Mahadevan [54] considered linear light absorption by assuming a proportional relationship between light intensity and photo-strain in order to derive the light-induced bending model. As light penetrates the LCE material, the light intensity decreases exponentially, leading to an exponential decay of light-induced strain. Since this linear absorption is not associated with the *trans-cis* transition, Corbett and Warner [55] investigated the photo-responsive mechanism by considering a non-linear absorption, which couples light intensity and a varying *tran*

13

fraction. However, these two models simply assumed Young's modulus as a constant value. In practice, Young's modulus is spatially dependent through the LCE thickness. Jin et al. [56] developed the gradient bending model by considering the photo-isomerization process and the nematic-isotropic phase transition. This model takes into account both the non-linear absorption and spatially dependent Young's modulus. However, the gradient bending model is time-implicit. Thus it is significant to develop a time-explicit model of LCE behavior for system-based implementation.

1.4 Research Objectives

Research objectives are to design a smart material selection tool and develop mathematical models where they don't exist. The software tool enables users to select material types and their corresponding geometric dimensions in the design of smart material devices.

Design of Software Interface: In this phase, information on the various aspects of smart materials is compiled in an easy-to-access format by conducting an extensive survey of published articles relevant to material properties. The collected material data encompasses potential applications and the system-level simulation models as well as material properties and material-level models. The types of smart materials include dielectric elastomers, liquid crystal elastomers, piezoelectric (polymer/ceramic) materials, shape memory (alloys/polymers), electro-rheological and magneto-rheological fluids, and thermoelectric materials. According to their functionalities, they are categorized into four groups: actuator, sensor, energy generator, and passive structural materials. The various properties of the materials in each group are characterized and compiled in a database.

14

Mathematical Modeling of Smart Materials, and Implementation in Software: Currently available mathematical models and potential applications are identified to select the best model for a given purpose. In cases where no suitable model for implementation is determined, an effective mathematical model is developed. The current and potential applications of the materials are addressed and the associated system-level models for selected materials are developed to show the performance of the overall system. Comprehensive databases on smart materials and their models are compiled into the material selection tool.

Evaluation of the Smart Material Selection Tool: The goal of this phase is to evaluate the effectiveness and accuracy of the data and the models in the smart material selection tool. The selected mathematical models from previous studies and newly developed models in the tool are validated by comparing this program's outputs with other published experimental results. Based on the results, the material and device models are improved. The experimental verification of the material models shows the reliable performance of the smart material design, modeling, and selection tool.

Additional Research on Light-Induced LCEs: This phase involves the development of a bending model and a time-explicit strain model on light-induced liquid crystal elastomers.

Chapter 2 : Smart Material Design, Modeling and Selection Tool: Polymers

The following subsections describe the work in the first two main phases mentioned above in detail.

2.1 Design of Software Interface, and Material Database

The software tool structure is illustrated in Figure 2.1. It is constructed with three distinct interfaces as follows: material database; design & modeling; and performance data.
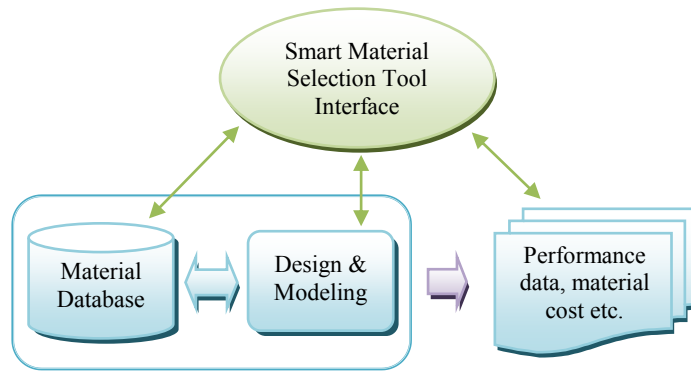
Figure 2.1. Structure of the Software Tool

Material databases are viewed as shown in Figure 2.2. The database interface provides users with the ability to add, delete, edit, and select content. The material databases are created in MS Access^{TM}. In the database, there are several tables which

include each material property or material type. The database displays data in a tabular format having rows and columns. The contents of all existing databases can be added, deleted, or modified from the tool. The ability to fully edit the database is provided in the user-defined environment. Thus, users can change databases to suit their specific needs. The compiled databases on smart materials are shown in the GUI-based computer software that determines and simulates what material to use based on properties and performance.
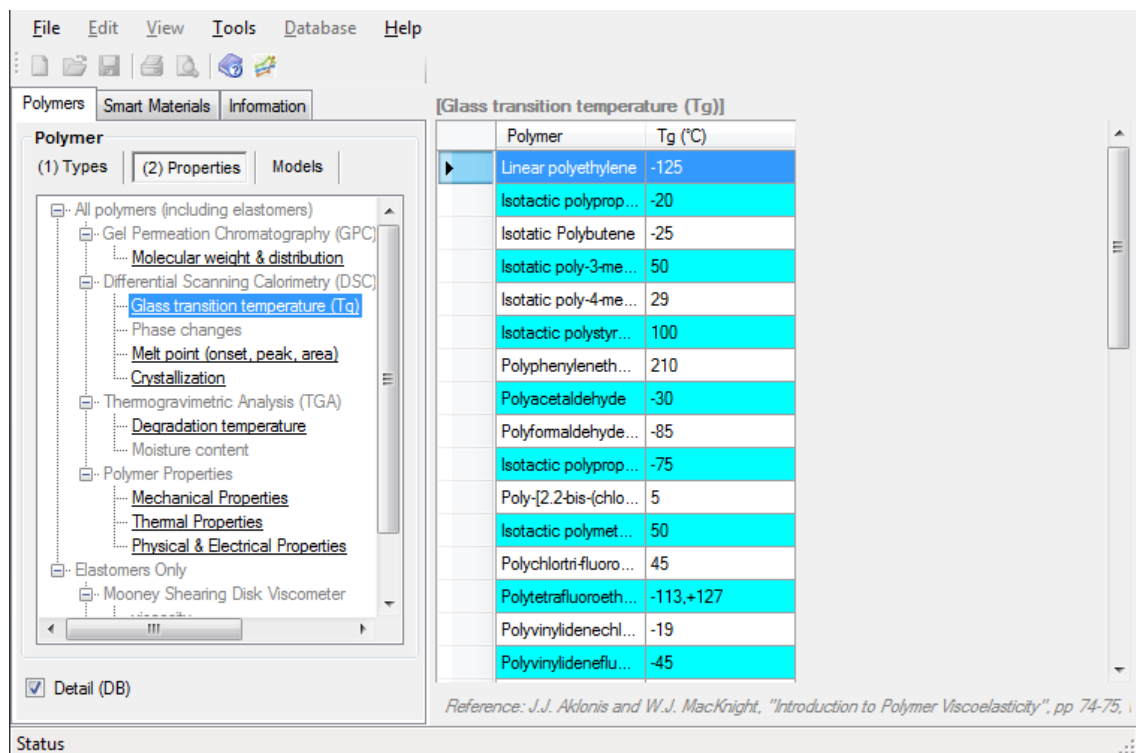
Figure 2.2. Polymer Properties listed in the TreeView and the Database shown in the DataGridView

The design and modeling interface enables users to specify model parameters and select a material type to be performed. Material data changes made in this interface are stored to corresponding material databases.

The performance data interface provides output values or plots as a result of design & modeling specifications and material database selection.

2.2 Mathematical Modeling of Smart Materials, and Implementation in Software

Material systems and models are designed to provide material performance. Table 2.1 shows the features in the material selection tool. The software has three main features: Polymers; Smart Materials; and Information.

Polymers	Types and Properties
	Models:
	  WLF Equation
	  Dielectric Elastomers
	  Liquid Crystal Elastomers

Smart Materials	Piezoelectric Actuators PVDF Shape Memory Alloys Shape Memory Polymers Thermoelectrics ER or MR Fluids
Information	External Databases Cost Info.
More Tools	Unit Conversion Material Chart

Table 2.1. Software Features

The contents of the material selection tool based on the GUI format consist of the following three sections: 1) Polymers (Polymer types and properties, Polymeric

behaviors including dielectric elastomers and liquid crystal elastomers); 2) Smart Materials (Piezoelectric ceramics/polymers, Shape Memory Alloys/Polymers, Thermoelectrics, ER or MR Fluids); 3) More information (External databases, Cost information, etc). These software features are contained in three different main tabs: "Polymers", "Smart Materials", and "Information".

2.2.1 Polymers

The "Polymers" tab on the upper left of Figure 2.3a-c has functions to show combined data of polymer types and properties, separate detailed data of polymer types and properties, and polymeric behaviors.
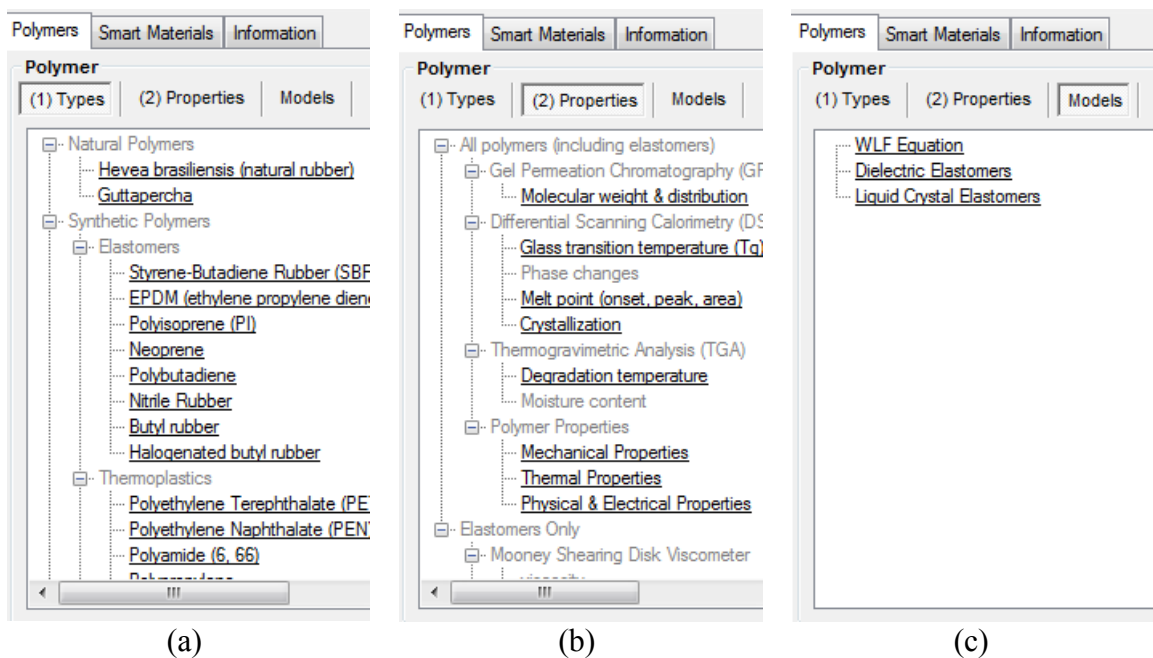
Figure 2.3. Three Sub-tabs under "Polymers" Main Tab: (a) "(1) Types", (b) "(2) Properties", and (c) "Models"

The "Polymers" tab in the tool has three sub-tabs: "(1) Types"; "(2) Properties"; and "Models". The first two sub-tabs provide database content relevant to polymer types and properties. The third sub-tab "Models" contains database and material models consisting of the Williams-Landel-Ferry equation (WLF equation), dielectric elastomers, and liquid crystal elastomers. The details are given in the following subsections and only liquid crystal elastomers are separately presented in Chapter 5.

2.2.1.1 Polymer types and properties

Polymer types are categorized as natural polymers, synthetic polymers, and biopolymers. The polymer properties include characteristics such as molecular weight distribution, glass transition temperature, melt temperature, crystallization, and degradation temperature. In addition, there are some mechanical, thermal, physical, and electrical properties of polymers. Polymer types and properties can be combined and viewed together by selecting items from the "(1) Types" and "(2) Properties" tabs. Additionally, separate detailed data of each type and property can be shown if the "Detail (DB)" checkbox is selected. In the TreeView, each node is editable and a new database can be created by users.

2.2.1.2 Polymeric behavior

For the "Models" tab, there are three components; the WLF equation, dielectric elastomers, and liquid crystal elastomers. The WLF equation is given to show polymeric behavior such as temperature dependency of a polymer's viscoelasticity [62].

$$\log a_T = \frac{-C_1\left(T - T_g\right)}{C_2 + \left(T - T_g\right)} \tag{2.1}$$

where a_T is a reference temperature, C_1 and C_2 are constant values, and T_g is a glass transition temperature. The parameter values can be defined by selecting a polymer type from the given database table or changed by inputting WLF parameter values in textboxes. The plot of the WLF equation is displayed on the right pane by clicking the "Calculate & Plot" button. The graph can be resized by changing the limit values in the textboxes. When the mouse pointer is moved on each label, a corresponding tooltip appears for users to understand each parameter.
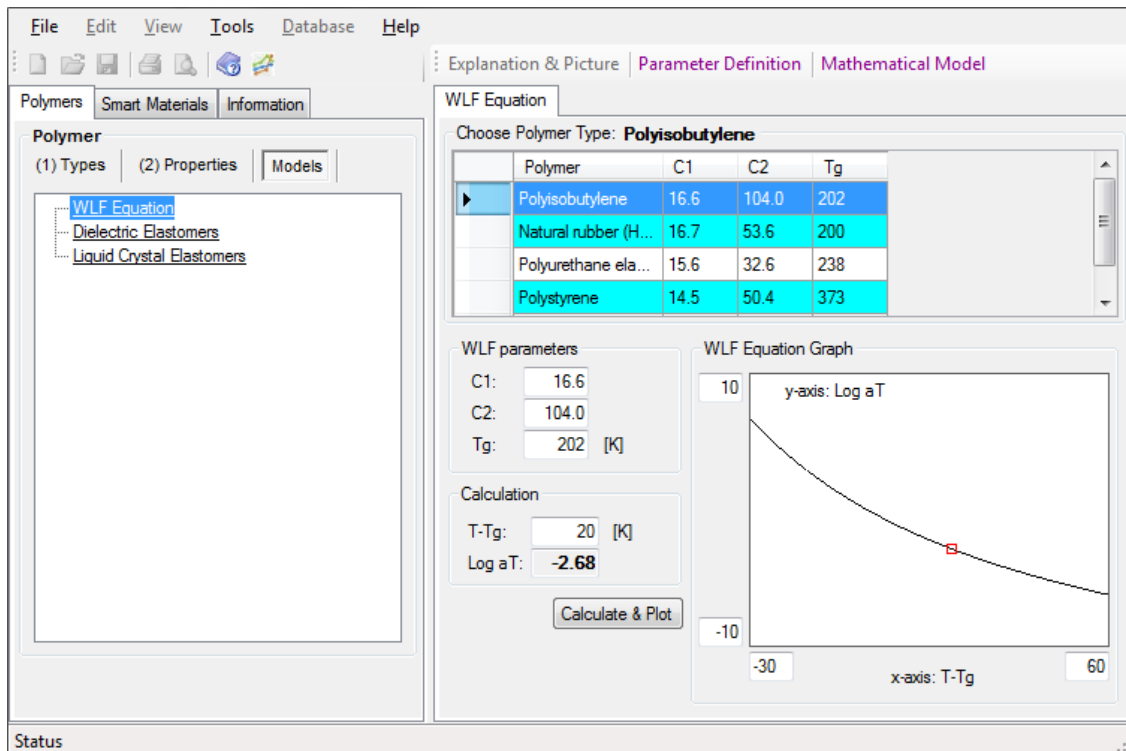
Figure 2.4. WLF Equation

2.2.1.3 Dielectric elastomers

Dielectric elastomers (DEs) consist of two compliant electrodes and a thin elastomer film [14]. The unique property of DEs is a high actuation strain in the presence of an applied voltage. A voltage, which is applied onto the electrodes, induces the deformation of the elastomer film. An electric force causes the film contraction along the electric field direction. Due to the contraction, the elastomer film elongates in the direction of the film.

The values of the dielectric elastomer film strain are plotted over a voltage range 0 – 2600 volts) shown in Figure 2.5. The force equilibrium equation is expressed in terms of tensile loading (F_t), Maxwell force ($F_{maxwell}$), and Ogden model (F_{Ogden}) as written in Equation (2.2). Tensile loading, which is initial pre-stretching, is applied in the perpendicular direction to the applied field. The Maxwell force, which is the mechanical driving force derived from Coulomb charge attraction, is obtained by taking a derivative of the energy density of the electric field and the thickness.

$$F_t + F_{maxwell} = F_{Ogden} \tag{2.2}$$

$$F_{maxwell} = \frac{x_2'}{x_3'} \varepsilon\varepsilon_0 V^2 \alpha \tag{2.3}$$

where F_t is tensile loading, ε is dielectric constant, and ε_o is vacuum permittivity. x_2' and x_3' are original width and original thickness, respectively. V is applied voltage and α is extension ratio.

The Ogden model [19] describes a wide range of strain hardening phenomenon of the rubberlike solid. In order to model the strain hardening effect, researchers have

introduced several strain-energy functions, which consist of principal stretch ratios, a strain hardening exponent and the interpretation of the shear modulus under infinitesimal straining [20, 21]. The evaluation of the strain–energy functions leads to obtaining the stress-strain relation. The Ogden model, which uses the strain energy function, is described in Equation (2.4) [17].

$$F_{Ogden} = x_2' x_3' \left[\mu_1 \left(\alpha^{k_1-1} - \alpha^{-1-k_1} \right) + \Theta \mu_2 \left((\lambda \alpha)^{k_2-1} - (\lambda \alpha)^{-1-k_2} \right) \right] \qquad (2.4)$$

where μ_1 and μ_2 are the Ogden materials constants. k_1 and k_2 represent any real number.

Θ is the switching function which gives 0 for low α and 1 for high α [16].

$$\Theta(\alpha) = \frac{1}{1 + \exp\left((\alpha_0 - \alpha)/\Delta\alpha\right)} \qquad (2.5)$$

where α_0 indicates the actuator extension ratio at the sprayed electrodes. $\Delta\alpha$ determines the switching width.

Numerical methods such as poly regression and root finding are coded in order to calculate the extension ratio at a given voltage input. The extension ratio is expressed in engineering strain and plotted in Figure 2.5. Thus, users can see how large of strain values can be obtained for a given DE film geometry, initial tensile loading, and voltage input.
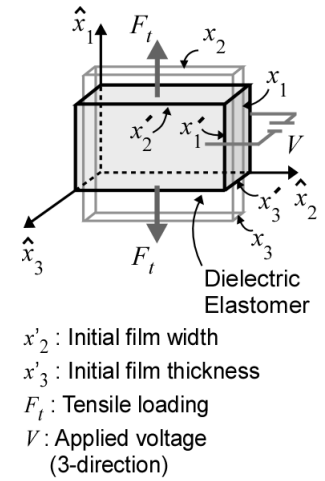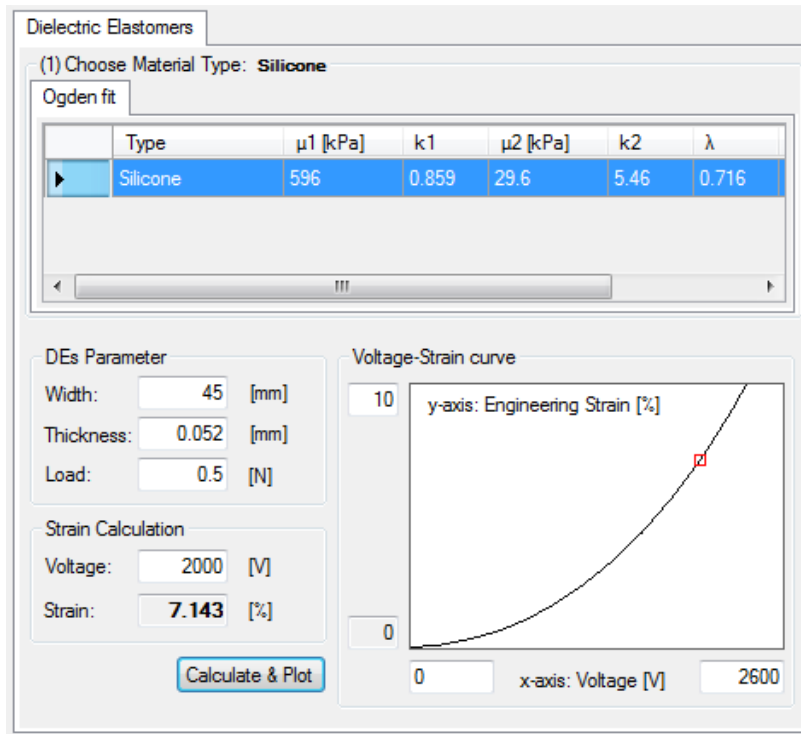
Figure 2.5. Dielectric Elastomers

Chapter 3 : Smart Material Design, Modeling and Selection Tool: Smart Materials and Information

3.1 Smart Materials

The "Smart Materials" tab, which is next to the "Polymers" tab shown in the upper left of Figure 2.2, provides information on the design of smart material devices. It is comprised of piezoelectric ceramics/polymers, shape memory alloys/polymers, thermoelectrics, and electrorheological (ER) and magnetorheological (MR) fluids as listed in Table 3.1.

Piezoelectric (ceramics/polymers)	Bimorph actuator Patch actuator Tubular actuator Multilayer stack actuator Rainbow/Thunder actuator Actuation and charge generation PVDF sensor
Shape Memory Alloys	Round wire Springs
Shape Memory Polymers	Stress-Strain-Temperature Relationship
Thermoelectrics	Power generator Heat pump
ER or MR Fluids	Shear mode dampers Flow mode dampers

Table 3.1. Smart Material Devices in the Selection Tool

3.1.1 Piezoelectric ceramics and polymers

Several piezoelectric actuators and sensors with different configurations are designed and modeled in the tool. Their lists are displayed inside the TreeView, which is positioned on the left pane of the tool window. On the right pane, there exist database tables (material types and property values), parameter inputs (geometry and applied inputs), and performance results (deflection, force, voltage, etc).
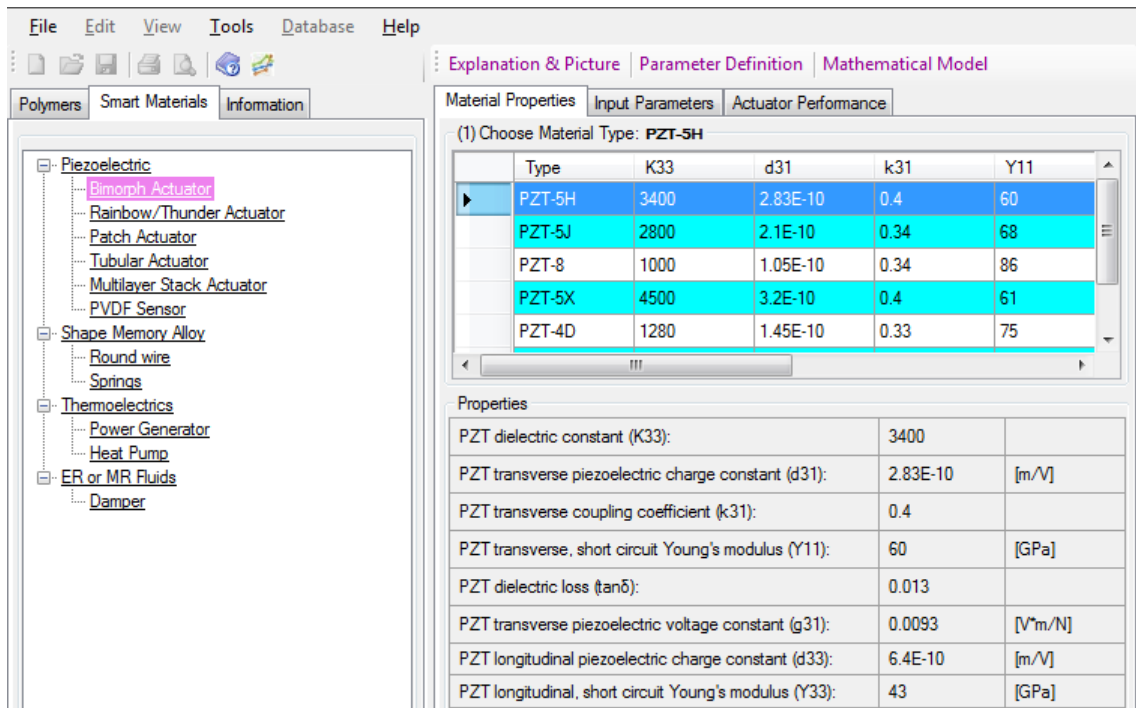
Figure 3.1. Bimorph Actuator

<table>
<tr><th colspan="3">Material Properties | Input Parameters | Actuator Performance</th></tr>
</table>

You have chosen
Material Type: PZT-5H

(2) Input Parameters:

Actuator length (L):	75	[mm]
Actuator width (w):	17.5	[mm]
Actuator thickness (t):	0.43	[mm]
Actuator drive voltage (V):	150	[V]
Frequency (f):	1	[herz]
PZT ceramic layer thickness (tc):	0.19	[mm]
Bimorph vane thickness (τ):	0.05	[mm]

(a)

Material Properties | Input Parameters | Actuator Performance

Performance

Parameter	Bimorph (Cantilever)	
Capacitance [nF]	103.98	
Current [mA]	0.1	
Electrical Power [mW]	14.89	
Deflection [µm]	2139.23	
Blocked Force [N]	0.11	
Max. Mechanical Power [mW]	0.73	
Max. Actuator Efficiency [%]	4.67	

(b)

Figure 3.2. (a) "Input Parameters" Tab and (b) "Actuator Performance" Tab

3.1.2 Bimorph, patch, tubular, and multilayer stack actuators

The magnitude of bending displacement is varied by the input voltage, material properties and actuator geometries. By incorporating these factors into the actuator model, the selection tool shows bending deflection, blocked force, and other performance as shown in Figure 3.2.

The following equation shows the bending deflection of a bimorph actuator [63] for each cantilever and simple beam case.

$$\Delta L = \begin{cases} 1.5g_{31}\left(L/wt\right)CV\left(1-\left(\tau^2/t^2\right)\right) & \text{Cantilever} \\ 0.375g_{31}\left(L/wt\right)CV\left(1-\left(\tau^2/t^2\right)\right) & \text{Simple beam} \end{cases} \quad (3.1)$$

where ΔL is bending deflection, g_{31} is transverse piezoelectric voltage constant, L is actuator length, w is actuator width, τ is bimorph vane thickness, and t is actuator thickness.

Bimorph, patch, tubular, and multilayer stack actuators are designed with the model given by Near C.D. [63]. Their performance is obtained by the following steps. The first step is to choose one of piezoelectric material types from the database in the "Material Properties" tab. Users can add their own material properties in the database. The next step is to fill values in the "Input Parameters" tab for actuator dimensions and driving inputs such as voltage and frequency. Then, based on the mathematical model, outputs are calculated and shown in the "Actuator Performance" tab. The main outputs are actuator deflection, blocked force, and maximum mechanical power.

For additional information, there are explanations with related images, parameter definitions, and mathematical models describing the actuators. Figure 3.3 shows the pop-up windows for this information.
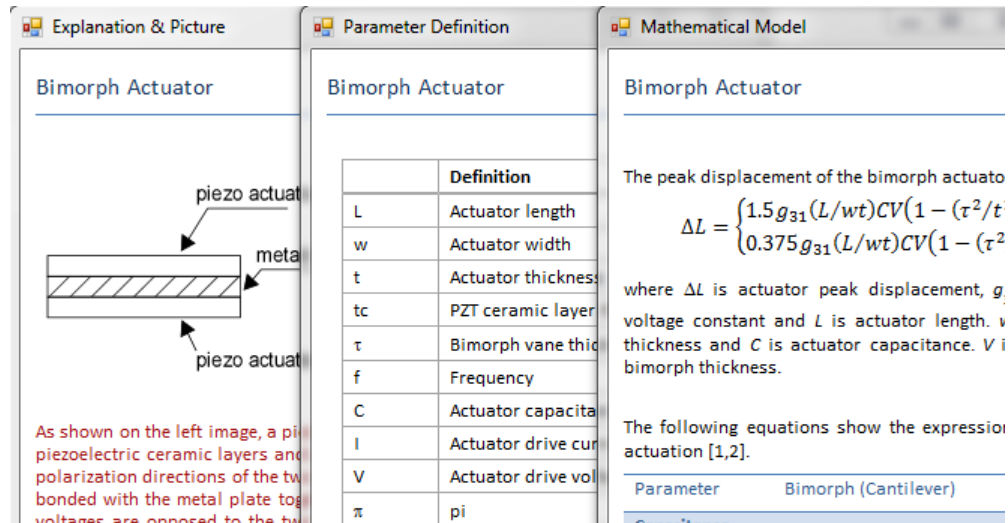
Figure 3.3. Explanation, Parameter Definition, and Model Description

3.1.3 Rainbow/Thunder actuator

Rainbow/Thunder actuators are composed of one active thin piezoelectric ceramic layer between a thin metal substrate on the bottom and an electrode on the top. This type of actuator, which consists of one active layer and one inactive layer, is called a unimorph. Both unimorphs and bimorphs are operated in a similar way. The deflection of a bimorph given by Anderson, E.H. [28] is employed to derive Equation (3.2).

$$w = \frac{M_\Lambda}{(YI)_{total}} \times \Phi \times \frac{l^2}{2} \tag{3.2}$$

where $\Phi = 1 - \frac{(2/t_b) \cdot (YI)_{total} \cdot (YS)_{total} - (YS)_{total} \cdot (YS)_{total}}{(YA)_{total} \cdot (YI)_{total} - (YS)_{total} \cdot (YS)_{total}}$, M_Λ is induced bending, $(YI)_{total}$ is bending stiffness, $(YS)_{total}$ is coupling stiffness, and l is length.

Figure 3.4. Actuation of Rainbow/Thunder

Figure 3.4 shows the actuation design of a Rainbow/Thunder actuator. For actuation, different material types can be selected for PZT from the "(1) PZT material" database and beam materials from the "(2) Beam material" database. In order to calculate the tip deflection of the beam, it is required to specify the input values shown in the "(3) Dimensions & Input Voltage" table.

In addition, this actuator produces charge when it is subjected to an applied force. As shown in Figure 3.5, the second tab is designed for charge generation of the actuator.

Figure 3.5. Charge Generation of Rainbow/Thunder

In this part, PZT and the substrate materials can be selected. Next, substrate and beam dimensions need to be filled in the "(3) Dimensions" table. The output value shows the calculation result of the generated charge.

The charge output value in the beam is calculated by the given Equation (3.3) [64].

$$q = -b e_{31} \left(\frac{z_3 + z_2}{2} \right) \int_0^a \frac{\partial^2}{\partial x^2} w(x) dx \qquad (3.3)$$

where q is charge generated in the beam and w is deflection in the z direction. z_2 is distance between interface of PZT and substrate from neutral surface. z_3 is distance between top of beam from neutral surface.

3.1.4 PVDF sensors
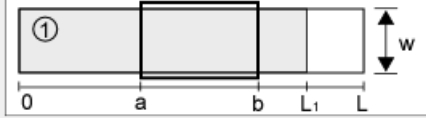
Polyvinylidene Fluoride (PVDF) is a piezoelectric polymer that exhibits a strong piezoelectric effect. As a sensor, it provides a relatively high voltage output in response to an external pressure. In order to obtain a charge output from the GUI-based tool, the following steps are required. First, one of the electrode types should be selected. There are two different electrode configurations such as rectangular or triangular in design. Second, input parameters are necessary to be added in the "(2) Input Parameters" GroupBox. Those values are the PVDF film dimension (length and width), electrode dimension, and applied load. The load force is uniformly distributed inside the thick rectangular region (from "a" to "b" in Figure 3.6). Next the PVDF film generates electrical charges which are picked up by the electrodes. Figure 3.6 shows the rectangular shape of the electrode and the output charge is displayed with output voltage. Equation (3.4) shows the output expressions [65].

$$Q(t) = d_{33} \int_D n(x) \cdot T_3(x,t) \, dx \quad \text{and} \quad V_0 = \frac{Q(t)}{C_{film}} \tag{3.4}$$

where Q is the total charge, $n(x)$ is the aperture shading function, T_3 is the applied stress, V_o is the output voltage and C_{film} is the capacitance of PVDF film.

Figure 3.6. Output Charge and Voltage of PVDF Sensor

3.1.5 Shape memory alloys

Shape memory alloys (SMAs) are alloys that possess the ability to remember their original shape. They can undergo considerable shape deformation at low temperatures and retain this deformation until they return to the pre-deformed shape upon heating above a certain transition temperature. SMAs are being used in variety of applications including SMA wire and spring designs [66, 67].

32

3.1.5.1 SMA wire

Figure 3.7 shows the stress-strain relation of an SMA wire. The following steps describe how to obtain strain values in an SMA wire from the tool. The first step is to choose a material type by clicking a row from the database. Next, the input boxes within "(2) material properties" GroupBox are filled with the properties of the chosen material type. The material properties are transformation temperatures (austenite and martensite start/finish temperatures As, Af, Ms, Mf), stress influence coefficients (Ca, Cm), Young's modulus in the austenitic and martensitic forms (Ea, Em), maximum recovery strain (eL), and critical stress (start and finish transformation (σs_cr and σf_cr)). 'a' and 'm' denote austenite and martensite, respectively. The next step is to select one of the SMA models from the ComboBox. There are three different models employed in the code: Tanaka, Liang & Rogers, and Brinson model.

The Tanaka model describes the thermomechanical constitutive equations and the transformation kinetics [37]. The equations of martensite volume fractions ξ are different for each model. In the code, inputs are temperature and stress. The input temperature indicates when an SMA material is initially austenitic. The output is the SMA wire strain. The equation for the transformation regions is given by

$$\left(\sigma - \sigma_0\right) = E\left(\xi\right)\left(\varepsilon - \varepsilon_0\right) + \Omega\left(\xi\right)\left(\xi - \xi_0\right) \tag{3.5}$$

where the subscript 'o' represents the initial condition of the SMA wire. E is the Young's modulus and Ω is the phase transformation coefficient.

From Equation (3.5), strain is derived as

$$\varepsilon = \frac{1}{E(\xi)}(\sigma - \sigma_0) + \varepsilon_L(\xi - \xi_0) + \varepsilon_0 = \frac{\sigma - \sigma_0}{E_A + \xi(E_M - E_A)} + \varepsilon_L(\xi - \xi_0) + \varepsilon_0 \qquad (3.6)$$

where ε_L is the maximum recoverable strain.

The Liang & Rogers model describes a unified thermo-mechanical constitutive law based on the Tanaka model. This model utilizes the same constitutive relationship that Tanaka used. The main difference arises in the development of the martensite volume fraction using the cosine function [38].

The Brinson model is derived based on the principles from the Tanaka model and the Liang & Rogers model. This model exhibits the desired characteristics such as critical stresses. The critical stresses at the start and end of the transformation are defined by the transformation equations of the Liang & Rogers model. These critical stresses are obtained by performing experiments on a particular SMA material. The critical stress values below Ms are assumed to be constant and are defined as σs_cr and σf_cr in the tool. In the Brinson model, the martensite volume fraction uses a modified cosine model and is divided into two parts such as applied stress part and temperature induced part [39]. After one of the SMA models is selected, the remaining step is to enter a temperature value for the SMA, which is initially austenitic, and an applied stress value within the "Strain Calculation" GroupBox. By clicking "Calculate & Plot" Button, the SMA wire strain values are plotted over the stress range and the two strain values corresponding at the given inputs are marked in rectangular shapes.
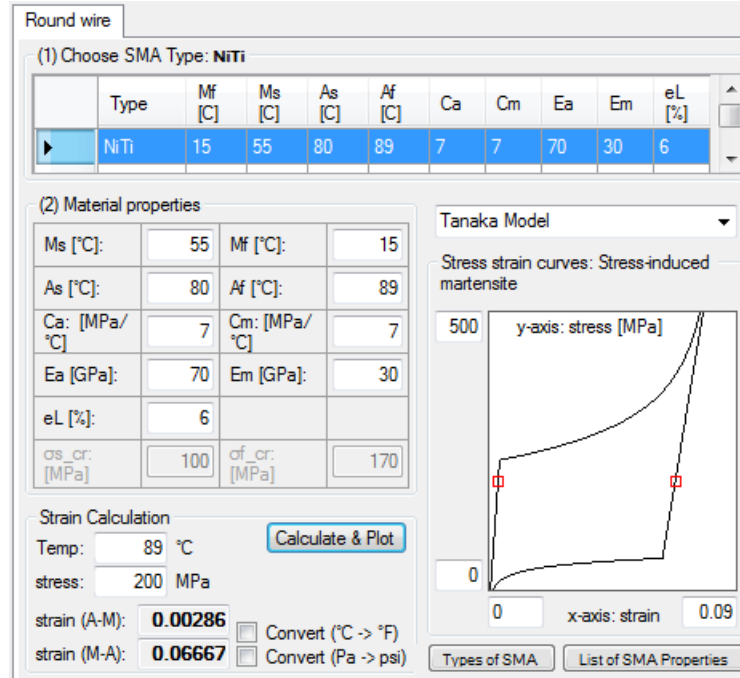
Figure 3.7. Stress-Strain Curves of SMA Wire

3.1.5.2 SMA spring

Shape memory alloys can be used in the form of springs. Figure 3.8 shows the design of the two-way actuation mode in which SMA springs extend when heated above austenite finish temperature and contract when cooled down below the martensite finish temperature [68]. For SMA springs, the design purpose is to determine the coil outer diameter (O.D.), wire diameter (d), and number of active coils (n) when the load on the spring and stroke length are given. An SMA material can be selected from the database.

$$d = \sqrt{\frac{8pc}{\pi\tau}}, \quad n = \frac{d\delta}{\pi\gamma D^2}, \quad O.D. = 6d \tag{3.7}$$

where p is the applied force, c is the spring index, τ is shear stress, δ is deflection, γ is shear strain, and D is spring average diameter.

Springs

(1) Device Requirement:
Load on spring (N):   15
Stroke length (mm):   20

(2) Design parameters of the Ti-Ni based SMA: **Ti-Ni-Cu**

	Type	max shear stress (GPa)	max shear strain (%)	shear modulus at high temp (GPa)	shear modulus at low temp (GPa)
	Ti-Ni (R-P...	0.12	1	23	8
▶	Ti-Ni-Cu	0.25	2	17	2

Below M_f Above A_f

p : Load on spring
δ : Stroke length
$O.D.$: Coil diameter
d : Wire diameter
n : Number of active coil

Calculated spring dimensions   [Calculate]
Coil diameter (mm):   **6.6**
Wire diameter (mm):   **1.1**
Number of active coils: **30**

Figure 3.8. Design of SMA Springs

3.1.6 Shape memory polymers

3.1.6.1 Standard linear viscoelastic model

A standard linear viscoelastic (SLV) model combines a spring and a Maxwell model in parallel and describes the mechanical properties of polymers which depend on time [60]. This model predicts both stress relaxation and creep. The Maxwell element is combined with the dashpot (damping ratio η) and the spring (stiffness E_1) in series.

36

Figure 3.9. SLV model

The stress and strain values in the Maxwell element are expressed as
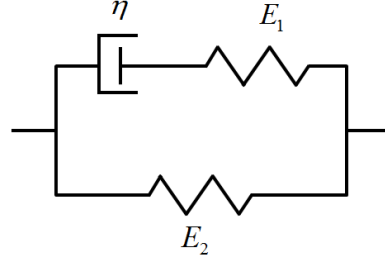
$$\sigma_m = \sigma_{s1} = \sigma_D \quad \text{and} \quad \varepsilon_m = \varepsilon_{s1} + \varepsilon_D \tag{3.8}$$

The total stress and strain of the SLV model are

$$\sigma_{total} = \sigma = \sigma_{s2} + \sigma_m \quad \text{and} \quad \varepsilon_{total} = \varepsilon = \varepsilon_{s2} = \varepsilon_m \tag{3.9}$$

where the subscript m, $s1$, $s2$, and D denote values in the Maxwell element, the upper spring (stiffness E_1), the lower spring (stiffness E_2), and the dashpot (damping ratio η), respectively. The stress value in each element is given by $\sigma_{s2} = E_2 \varepsilon$, $\sigma_{s1} = E_1 \varepsilon_{s1}$,

$$\sigma_D = \eta \frac{d\varepsilon_D}{dt}.$$

Then, the total stress is

$$\varepsilon = \varepsilon_m = \varepsilon_{s1} + \varepsilon_D = \frac{\sigma_{s1}}{E_1} + \frac{1}{\eta}\int \sigma_D dt = \frac{\sigma_m}{E_1} + \frac{1}{\eta}\int \sigma_m dt \tag{3.10}$$

By substituting $\sigma_m = \sigma - \sigma_{s2} = \sigma - E_2 \varepsilon$,

$$\varepsilon = \frac{1}{E_1}(\sigma - E_2\varepsilon) + \frac{1}{\eta}\int(\sigma - E_2\varepsilon)dt = \frac{\sigma}{E_1} - \frac{E_2}{E_1}\varepsilon + \frac{1}{\eta}\int(\sigma - E_2\varepsilon)dt$$

$$\left(\frac{E_1 + E_2}{E_1}\right)\varepsilon = \frac{\sigma}{E_1} + \frac{1}{\eta}\int(\sigma - E_2\varepsilon)dt \rightarrow \varepsilon = (E_1 + E_2)^{-1}\left[\sigma + \frac{E_1}{\eta}\int(\sigma - E_2\varepsilon)dt\right] \tag{3.11}$$

By taking the derivative with respect to time,

$$\frac{d\varepsilon}{dt} = \left(E_1 + E_2\right)^{-1} \left(\frac{d\sigma}{dt} + \frac{E_1}{\eta}\sigma - \frac{E_1 E_2}{\eta}\varepsilon\right)$$

(3.12)

$$\dot{\varepsilon} = \frac{1}{E_1 + E_2}\dot{\sigma} + \frac{E_1}{\eta(E_1 + E_2)}\sigma - \frac{E_1 E_2}{\eta(E_1 + E_2)}\varepsilon$$

$$\dot{\varepsilon} = \frac{\dot{\sigma}}{E} + \frac{\sigma}{\mu} - \frac{\varepsilon}{\lambda}$$

(3.13)

where $E = E_1 + E_2$, $\mu = \dfrac{\eta(E_1 + E_2)}{E_1}$, and $\lambda = \dfrac{\eta(E_1 + E_2)}{E_1 E_2}$.

3.1.6.2 Modified linear model

Shape memory polymers (SMPs) are in a glassy state exhibiting a high modulus at temperatures below T_g while it is in a rubbery state with a low modulus above T_g. Tobushi et al. [61] approximate the relationship between Young's modulus and temperature as shown in Figure 3.10.
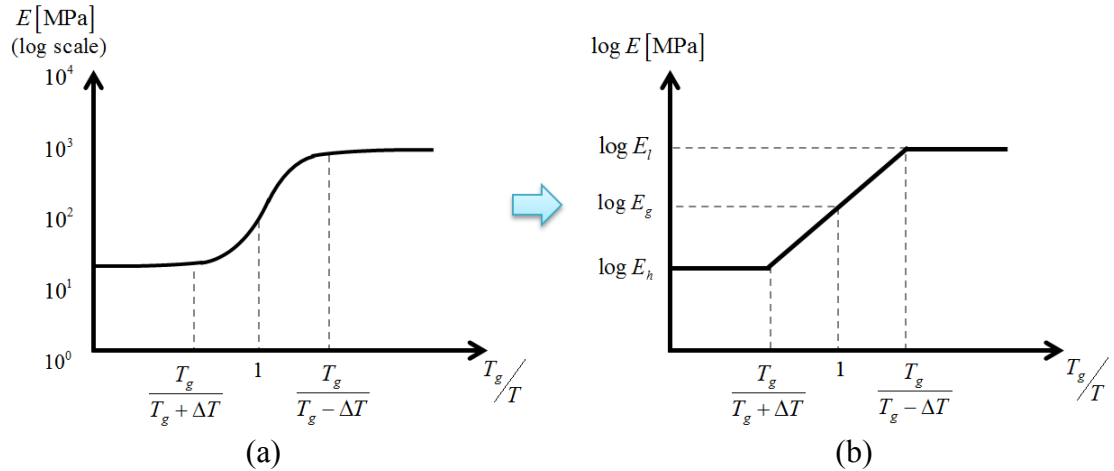
Figure 3.10. Young's Modulus vs. Temperature: (a) E [MPa] and (b) log$E$ [MPa]

Based on the linearized approximation shown in Figure 3.10, Tobushi et al. derive the relationship with an exponential term shown in Equation (3.14).

$$E = E_l \qquad\qquad\qquad \text{when } T < T_g - \Delta T$$

$$E = E_g \exp\left[a\left(\frac{T_g}{T} - 1 \right) \right] \quad \text{when } T_g - \Delta T \leq T \leq T_g + \Delta T \qquad\qquad (3.14)$$

$$E = E_h \qquad\qquad\qquad \text{when } T_g + \Delta T < T$$

where a denotes the slope of the glass transition region which is the straight line in Figure 3.10b. E_l and E_h are Young's modulus at a low temperature and a high temperature, respectively. E_g is Young's modulus at $T = T_g$. ΔT is the temperature half-width of the glass transition region.

SMPs exhibit a large variation in mechanical properties including creep recovery in the glass transition region. Figure 3.11 illustrates a creep strain and creep recovery at $T > T_h$ and $T < T_g$, respectively.

Figure 3.11. Creep and Creep Recovery: (a) $T > T_h$ and (b) $T < T_g$

T_h is a high temperature above T_g. The applied constant stress is removed at time t_1. The creep strain and creep recovery of SMPs behave like the SLV model when a temperature is greater than T_h as shown in Figure 3.11a. However, the SLV model cannot

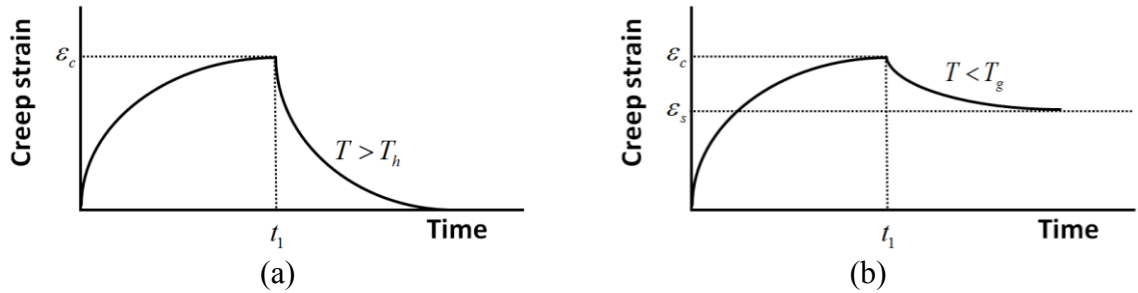predict the behavior shown in Figure 3.11b which shows the creep recovery below a glass transition temperature [59]. In order to describe the creep recovery at $T < T_g$, Tobushi et al. [59] proposed a four element model shown in Figure 3.12.
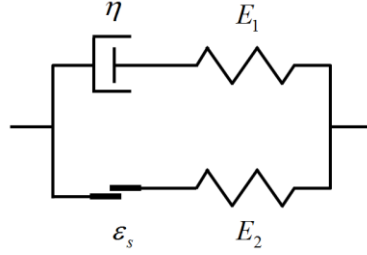
Figure 3.12. Modified Linear Four Element Model including a Slip Mechanism [59]

Tobushi et al. add one more element expressing a slip mechanism (ε_s) to the SLV model. This modified linear model is expressed as

$$\dot{\varepsilon} = \frac{\dot{\sigma}}{E} + \frac{\sigma}{\mu} - \frac{\varepsilon - \varepsilon_s}{\lambda} + \alpha \dot{T} \tag{3.15}$$

where E, μ, λ, and α represent modulus of elasticity, viscosity, retardation time and coefficient of thermal expansion, respectively. The slip mechanism ε_s is given by

$$\varepsilon_s = C\left(\varepsilon_c - \varepsilon_l\right) \tag{3.16}$$

where ε_s, ε_c, and ε_l are irrecoverable strain, creep strain, and critical value strain, respectively. C is irrecovery strain constant.

The stress differential equation is derived from Equation (3.15).

$$\dot{\sigma} = E\left[\dot{\varepsilon} - \frac{\sigma}{\mu} + \frac{\varepsilon - \varepsilon_s}{\lambda} - \alpha \dot{T}\right] = -\frac{E}{\mu}\sigma + \left[E\dot{\varepsilon} + \frac{E}{\lambda}(\varepsilon - \varepsilon_s) - E\alpha\dot{T}\right] \tag{3.17}$$

40
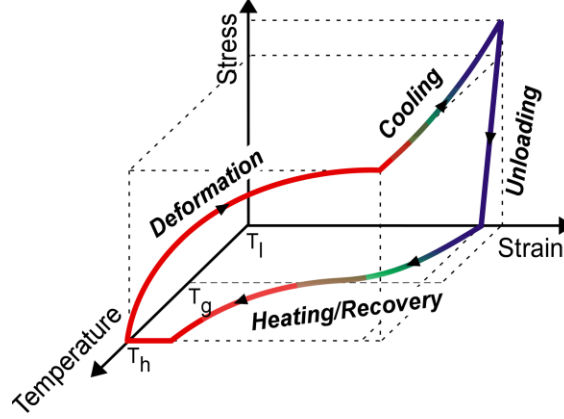
Figure 3.13. Typical Operating Cycle of SMPs

In a typical operating cycle, as shown in Figure 3.13, SMPs start at high temperature T_h. In the "Deformation" process, the maximum strain is applied while temperature keeps T_h. During the "Cooling" process, the maximum strain maintains constant and SMPs are cooled to T_l. In the "Unloading" process, the stress is removed at T_l. It is then heated from T_l to T_h as shown in the "Heating/Recovery" process of Figure 3.13. There is irrecoverable strain at T_h. The irrecoverable strain is recovered gradually with lapses of time under no-load at T_h. The irrecoverable strain at T_h depends on the heating rate [61]. If the heating rate is low, the irrecoverable strain becomes zero.

In the deformation phase, $\dot{T}$ is 0 at $T=T_h$. Equation (3.17) becomes

$$\dot{\sigma} = -\frac{E}{\mu}\sigma + \left[E\dot{\varepsilon} + \frac{E}{\lambda}(\varepsilon - \varepsilon_s)\right] \tag{3.18}$$

The stress-strain, stress-temperature, and strain-temperature relationships of the operating cycles are plotted in Figure 3.15a-b and Figure 3.16. In the relationships, an applied maximum strain ε_{max} is 4%. Loading strain rate, $\dot{\varepsilon}$ is 5/6 [%/s] and constant. State

41

variables x_1 and x_2 are σ and ε, respectively. Then, Equation (3.18) can be written with initial conditions and state variables.

$$x_1(0) = 0, x_2(0) = 0 \text{ and } \dot{x}_1 = \dot{\sigma}, \dot{x}_2 = \dot{\varepsilon}$$

$$\dot{x}_1 = -\frac{E}{\mu}x_1 + \frac{E}{\lambda}x_2 + \left[E\dot{\varepsilon} - \frac{E}{\lambda}\varepsilon_s\right]$$ (3.19)

In the cooling phase, strain rate $\dot{\varepsilon}$ is 0 at $T=T_l$. Cooling rate, $\dot{T}$ is -4K/min and constant. The stress differential equation is

$$\dot{\sigma} = -\frac{E}{\mu}\sigma + \frac{E}{\lambda}(\varepsilon - \varepsilon_s) - E\alpha\dot{T}$$ (3.20)

State variables x_1 and x_2 are σ and T, respectively.

$$x_1(0) = \sigma_{phase1-end}, \ x_2(0) = T_h \text{ and } \dot{x}_1 = \dot{\sigma}, \dot{x}_2 = \dot{T}$$

$$\dot{x}_1 = -\frac{E}{\mu}x_1 + \frac{E}{\lambda}(\varepsilon - \varepsilon_s) - E\alpha\dot{x}_2$$ (3.21)

In unloading phase, $\dot{T}$ is 0 at $T=T_l$. Unloading strain rate, $\dot{\varepsilon}$ is 5/6 [%/s].

$$\dot{\sigma} = -\frac{E}{\mu}\sigma + E\dot{\varepsilon} + \frac{E}{\lambda}(\varepsilon - \varepsilon_s)$$ (3.22)

State variables x_1 and x_2 are σ and ε.

$$x_1(0) = \sigma_{phase2-end}, \ x_2(0) = \varepsilon_{max} \text{ and } \dot{x}_1 = \dot{\sigma}, \dot{x}_2 = \dot{\varepsilon}$$

$$\dot{x}_1 = -\frac{E}{\mu}x_1 + E\dot{\varepsilon} + \frac{E}{\lambda}(x_2 - \varepsilon_s)$$ (3.23)

In heating and recovery phase, $\dot{\sigma}$ is 0. Heating rate is 4K/min.

$$\sigma = \mu\dot{\varepsilon} + \frac{\mu}{\lambda}(\varepsilon - \varepsilon_s) - \mu\alpha\dot{T}$$

$$\dot{\varepsilon} = -\frac{1}{\lambda}(\varepsilon - \varepsilon_s) + \alpha\dot{T}$$ (3.24)

State variables x_1 and x_2 are ε and T, respectively.

42

$$x_1(0) = \varepsilon_{phase3-end}, \ x_2(0) = T_l \text{ and } \dot{x}_1 = \dot{\varepsilon}, \ \dot{x}_2 = \dot{T}$$

(3.25)

$$\dot{x}_1 = -\frac{1}{\lambda}(x_1 - \varepsilon_s) + \alpha\dot{T}$$

Typical properties of Polyurethane-SMP are given in Table 3.2. T_g is 328K (54.85°C).

Coefficient	$T \le T_g$ -15K	$T \ge T_g$+15K
E [MPa]	907	27.6
μ [GPa·s]	116	2.03
λ [s]	2840	111
C [-]	0.716	0.0206
ε_l [%]	0.0184	3.83
α [K^{-1}]	11.6×10^{-5}	

Table 3.2. Properties of Polyurethane-SMP at $T \le T_g$ -15K and $T \ge T_g$+15K [59]

In Table 3.2, the values of coefficients can be obtained from the relationship of Equation (3.14) and values given in Table 3.3 and Table 3.4.

E_g [MPa]	μ_g [GPa·s]	λ_g [s]	C_g [-]	ε_g [%]
146	14	521	0.112	0.3

Table 3.3. Coefficients at T_g [59]

a_E	a_μ	a_λ	a_C	a_ε
38.1	44.2	35.4	38.7	58.2

Table 3.4. Slope values of the glass transition region [59]

Values of coefficients and slopes are added in the database shown in Figure 3.14. The equations corresponding four different phases of the modified linear model are incorporated into the software.
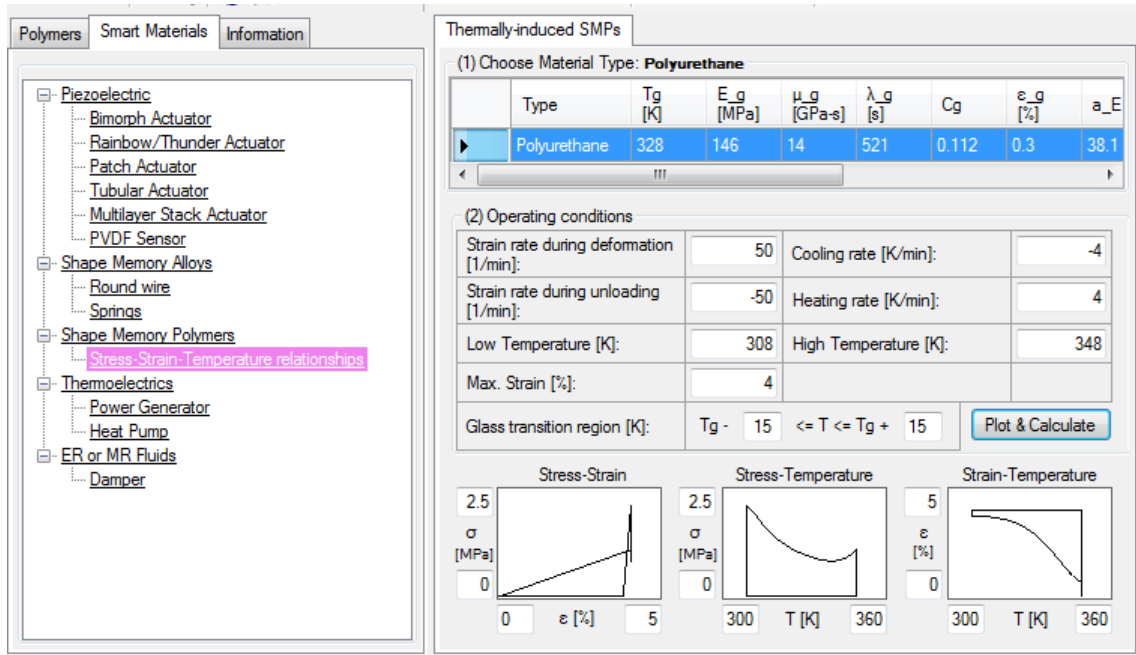
43

Figure 3.14. Software Interface for Shape Memory Polymers
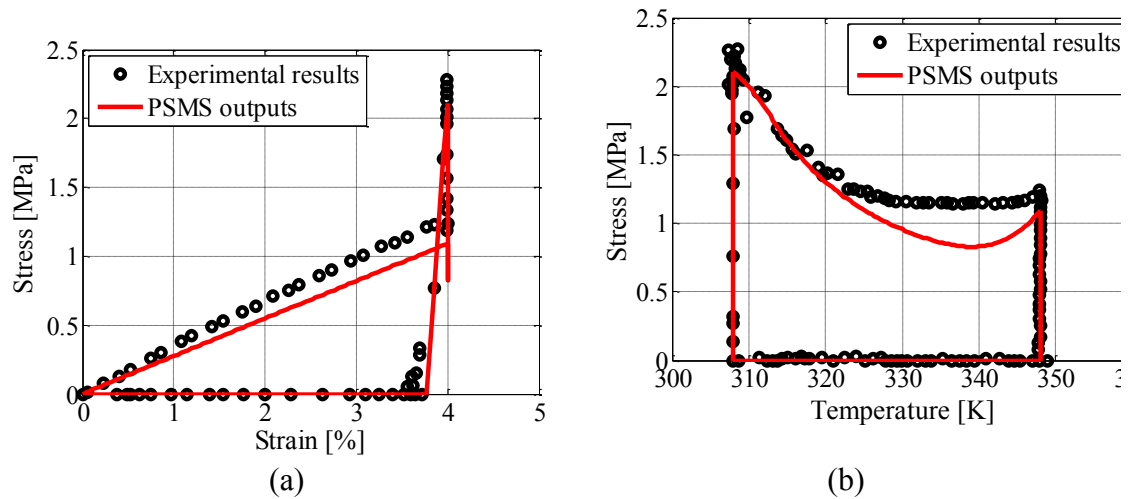
Figure 3.15. (a) Relationship between Stress and Strain at ε_m=4%, (b) Relationship between Stress and Temperature at ε_m=4% (Experimental Results [59])
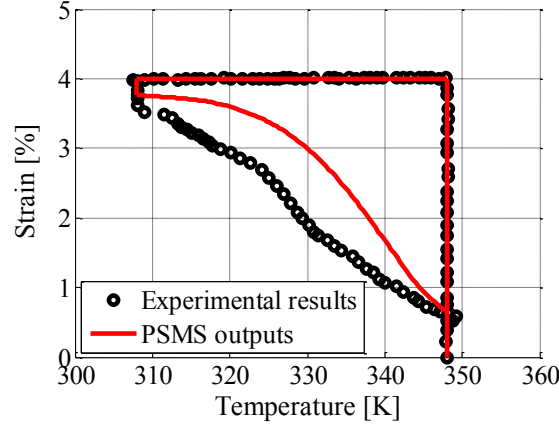
Figure 3.16. Relationship between Strain and Temperature at ε_m=4% (Experimental Results [59])

The three calculated plots shown in Figure 3.15a-b and Figure 3.16 are produced by using Equations (3.18)-(3.24). The model results are plotted with published experimental data [59]. The modified linear model expresses well the stress-strain and stress-temperature relationships when compared to experimental results as shown in Figure 3.15. However, the model has a problem in representing the strain recovery behavior in the strain-temperature relationship as shown in Figure 3.16. In order to express the large strain recovery, Tobushi et al. developed a nonlinear thermomechanical constitutive model which adds a nonlinear term to the SLV model [61].

3.1.7 Thermoelectrics

3.1.7.1 Thermoelectric power generator

The design purpose of the "Power Generator" tab is to calculate the minimum number of modules which satisfy the power requirement given in the "(1) Requirement"

45

GroupBox. Input parameters are temperatures on the hot side and the cold side of a thermoelectric module. One of the module types can be selected from the ComboBox in the "(3) Module Selection" GroupBox. Each module type contains the data of effective module parameters at various temperatures. Module material parameters are S_M, R_M, and K_M. S_M is the module's average Seebeck coefficient in volts/K, R_M is the module's average resistance in ohms, and K_M is the module's average thermal conductance in watts/K. These values are displayed with the dimensionless figure of merit, ZT. S_M and R_M are plotted over the range of average module temperature from 173.2K to 423.2K.
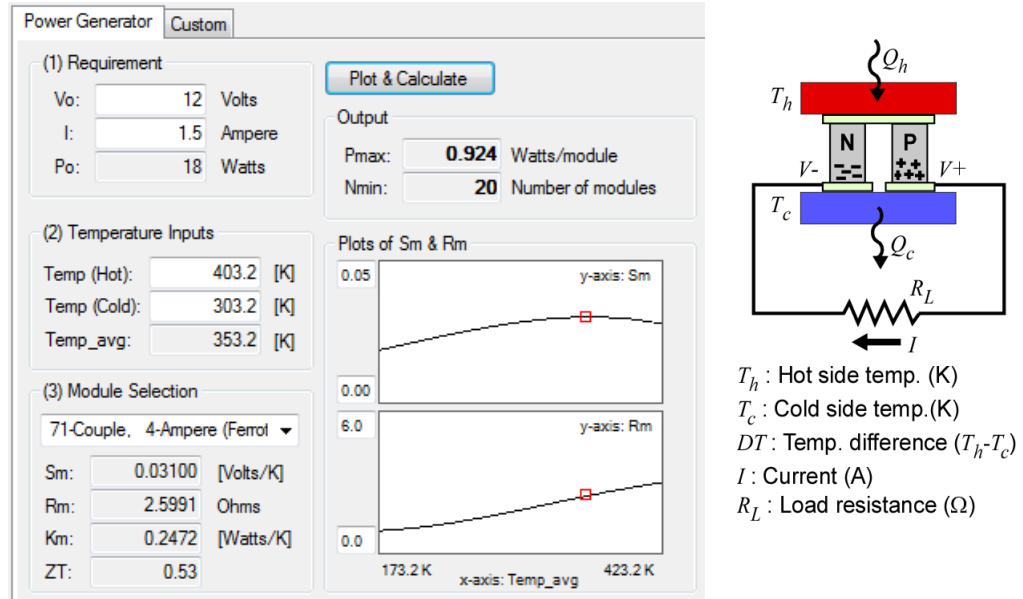
Figure 3.17. Thermoelectric Power Generator

In Figure 3.17, the output results are the maximum power produced by one module and the minimum number of modules needed to meet the power requirement. The maximum output power P_{max} of one module is expressed in the following equation.

$$P_{max} = \frac{(S_M DT)^2}{4R_M} \qquad (3.26)$$

3.1.7.2 Thermoelectric heat pump

Thermoelectrics can be used also as a heat pump, with an applied voltage causing heat to be absorbed at one side and expelled at the other. The heat pump can operate in either cooling or heating mode, depending on the polarity of the applied voltage. The design of the "Heat Pump" tab is displayed in Figure 3.18.
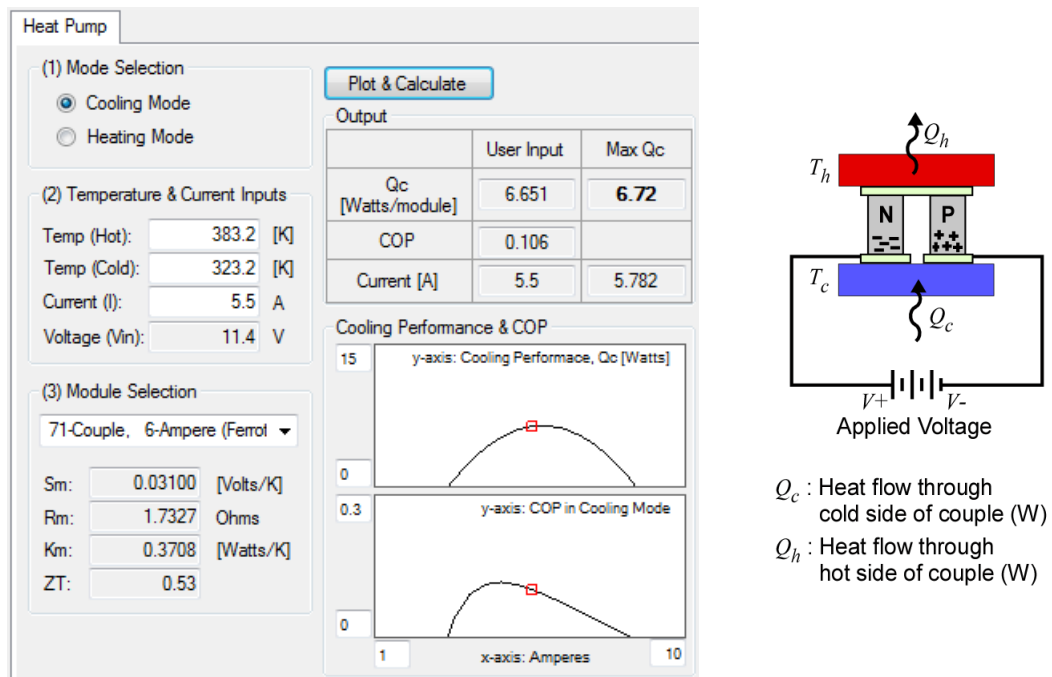
Figure 3.18. Heat Pump of Thermoelectric

Temperature and current are important inputs to the thermoelectric modules. After selecting a module type and filling in information about temperature and current, the heat flow is calculated [69]. In the cooling mode operation, the heat flow at temperature (T_c) is

$$Q_c = S_M T_C I - 0.5 I^2 R_M - K_M DT \tag{3.27}$$

In the heating mode, the heat flow at temperature (T_h) is

$$Q_h = S_M T_h I + 0.5 I^2 R_M - K_M DT \tag{3.28}$$

Figure 3.19 shows heating performance and coefficient of performance (COP) at fixed T_c and three different T_h values. When the temperature difference of T_c and T_h increases, heating performance and COP in heating mode drop.

Figure 3.19. Heating Performance and COP at Fixed T_c and Increasing T_h

3.1.8 ER and MR fluids

Figure 3.20 shows the application of ER or MR damper [70]. Shear mode and flow mode types are applied for the damper mode operations of ER/MR fluids. In shear

48

mode, the inner shaft of the damper generates damping forces through shearing of the fluids. In the case of Bingham plastic flow, the shear stress τ in damper shear mode modeling is expressed as [71]

$$\tau = \mu \frac{v_0}{d} + \tau_y \tag{3.29}$$

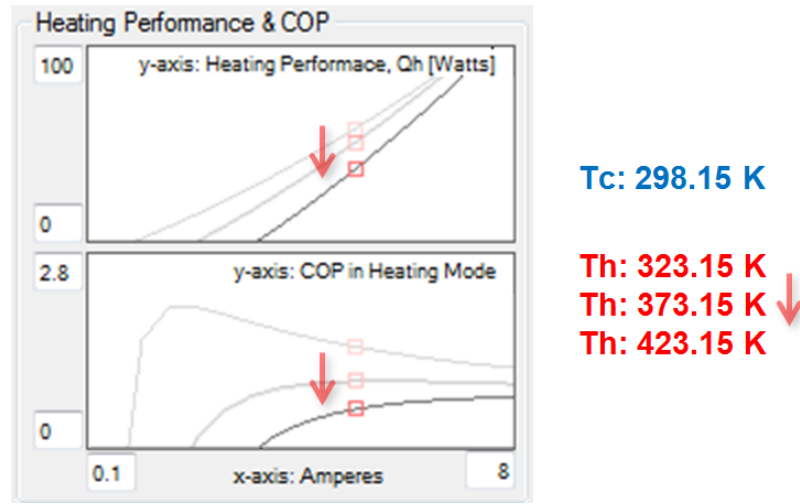where μ is the plastic viscosity, v_0 is the velocity at the boundary condition, and τ_y is the dynamic yield stress.

In flow mode, the piston head moves along the inner electrode. The inner and outer electrodes are tubes of circular cross section. In the case of Newtonian flow, the damper flow mode modeling is written as

$$\tau(y) = 6\mu \frac{v_0}{d^2} \left(\frac{A_p}{A_d}\right)^2 (d - 2y) \tag{3.30}$$

where A_p is the area of the piston head, A_d is the cross sectional area between the electrodes, and y is the latitudinal (electrode gap axial) coordinate.

Different types of ER or MR fluids can be selected from the "(2) Fluid Selection" GroupBox. Next, damper dimensions are determined by specifying the values of electrode gap, circumference, wetted electrode length, cross sectional area, and area of the piston head. Inputs are an electrical or a magnetic field, and v_0. The shear stress output is plotted over input field values in Figure 3.20.

49
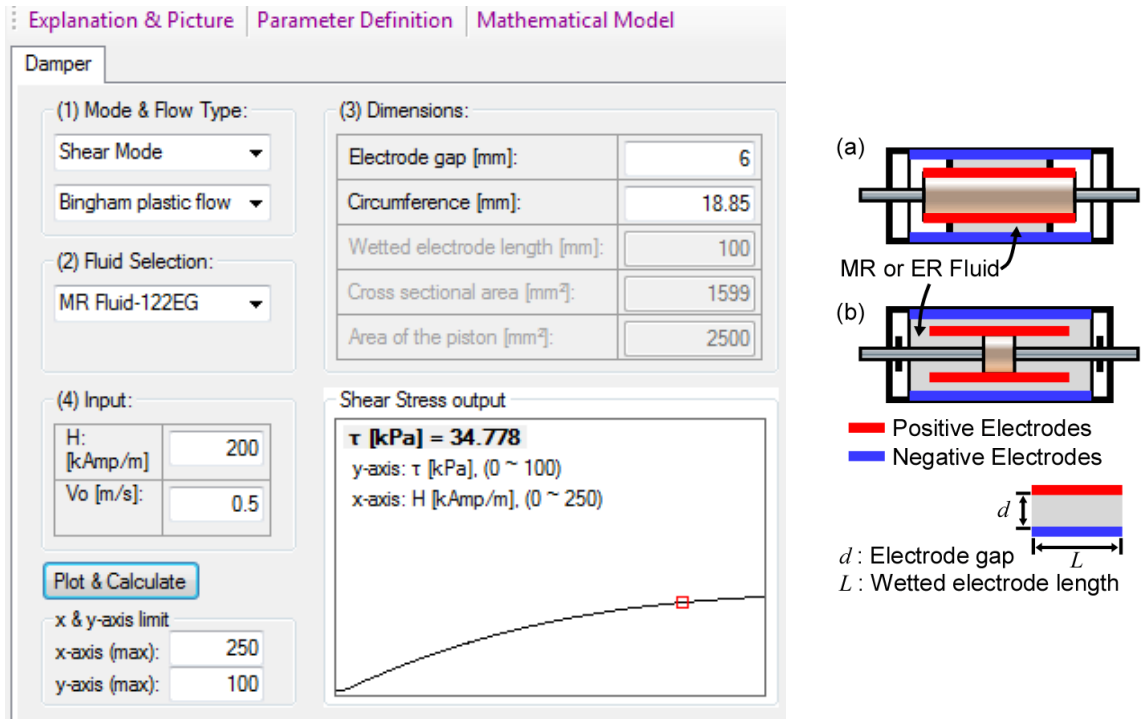
Figure 3.20. Damper Design of ER or MR Fluids

3.2 Information

Users may want to find more data which is not compiled in the tool. The subsection shows information such as external databases and cost. Unit conversion and tutorial pages are additionally given and discussed after that.

The "Information" tab is the third main tab and positioned to the right of the "Smart materials" tab. Under the "Information" tab, there are two active nodes: Web Links for external databases and Cost. Users can access external databases by clicking a row in a database table and then the "Database Information" tab displays a corresponding web page on the program pane. The external databases contain a broad range of material properties for polymers and smart materials. Users can connect to all of the other databases. The program window can be expanded enough to show the entire web page.
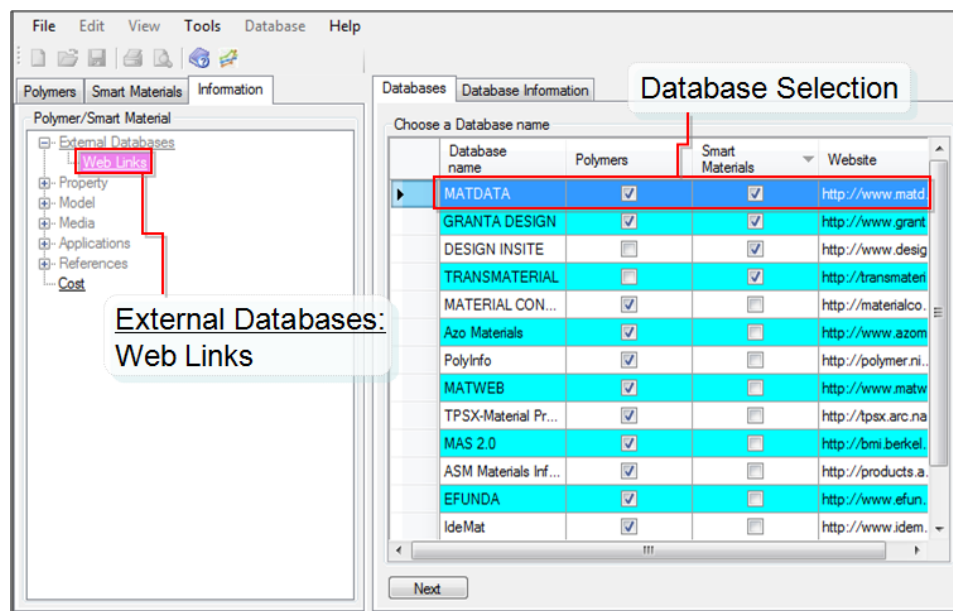
Figure 3.21. External Databases
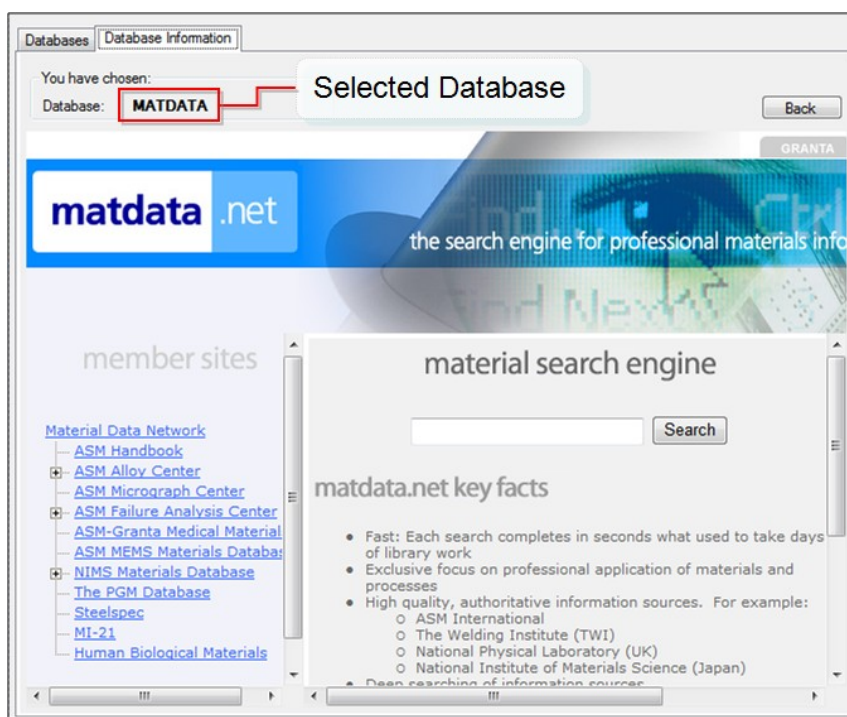
Figure 3.22. Selected External Database

Material cost is important in the aspect of deciding on cost effective materials. The cost information is given based on commercial products. There are lists of manufacturers and smart material types in the "Choose a Manufacturer" table. Lists of manufacturers can be sorted by types of smart materials. In the same manner shown in the case of the "External databases" node, "Cost" node also displays its selected company's cost relevant web page on the program pane. Users can find material cost information for smart materials as shown in Figure 3.23. When one of the manufacturers is selected, the "Cost Information" tab shows the corresponding company's website. Figure 3.17 is an example for MR fluid from LORD Corporation.
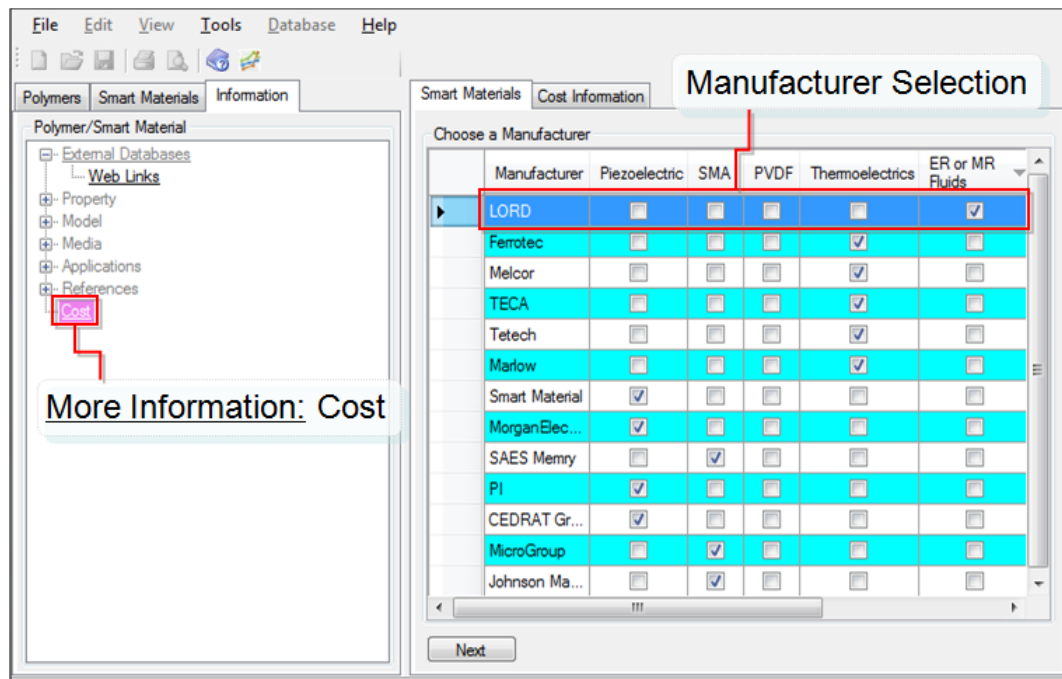
Figure 3.23. Lists of Manufacturers for Cost Information
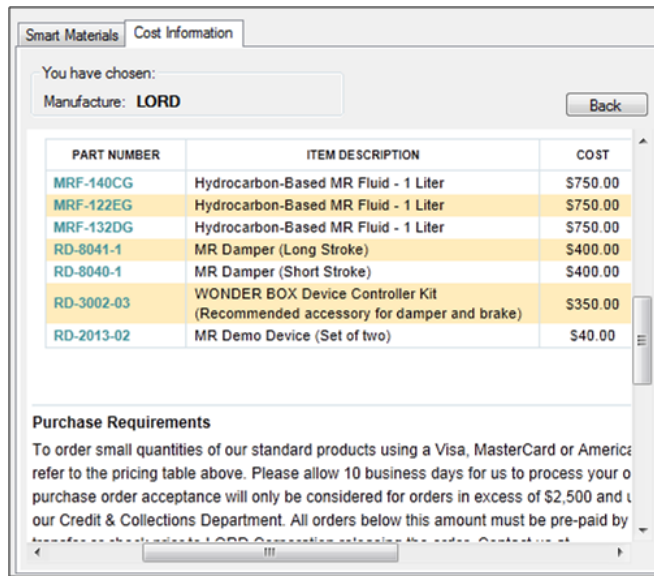
Figure 3.24. Selected Manufacturer's Cost Information

Unit conversion and tutorials are available under the menu bar. The unit converter provides the most frequently used conversions.
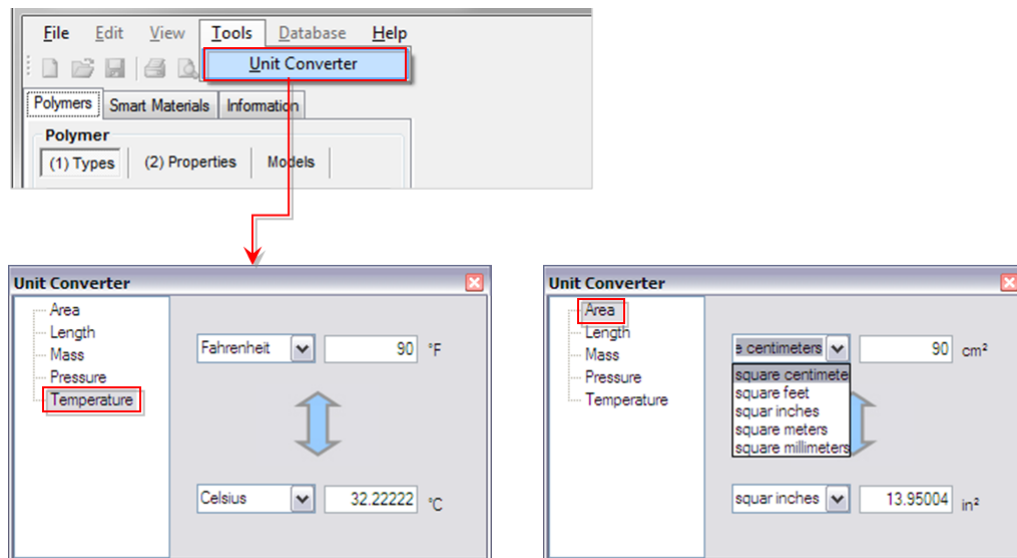
Figure 3.25. Unit Conversion

The "Tutorial" link under the "Help" menu can guide users to understand how the tool performs. Detailed explanations and instructions are provided to help users understand the material database tool.
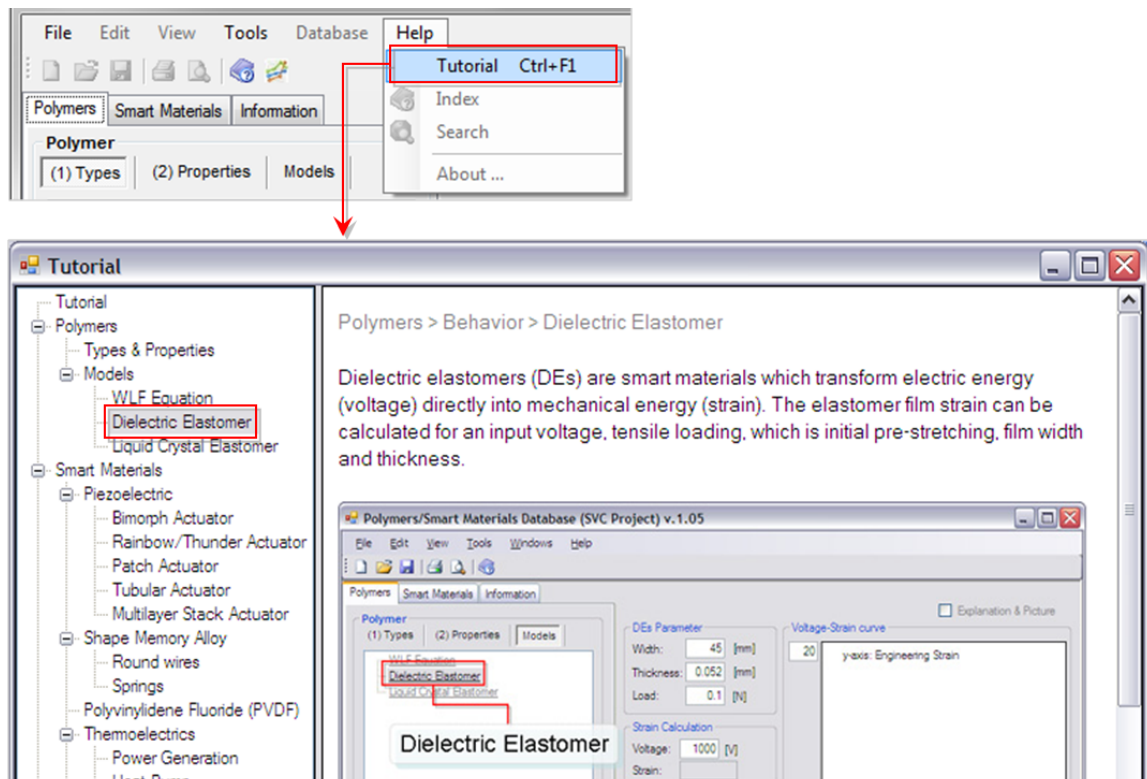
Figure 3.26. Tutorial

Chapter 4 : Evaluation of the Smart Material Selection Tool

The evaluation process shows the validation of the tool. Performance verifications of the selection tool are evaluated by comparing with available experimental results from other published articles. This chapter consists of examples, Section 3.1, and material and performance chart, Section 3.2.

4.1 Examples

The examples highlighted below show how the software can be used to design smart material systems. Actual examples of deployed products or patented devices are highlighted.

4.1.1 Dielectric elastomers

The engineering strain of DE film configured as a rectangular shape is induced by applying voltage through the electrodes on both sides of the film and initial tensile loading. In order to evaluate the software performance for DEs, the voltage-strain curve of the silicone DEs film is given from experimental tests conducted by Kofod [17] and compared with the PSMS outputs.

Kofod measured the deformed length of a silicone DE actuator using a force feedback procedure while the actuator was mounted on a test bench and applied from 0V to 2600V. The loading weight was varied from 5g to 130g. The original length was 15mm and the engineering strain for the silicone DE actuator was plotted by using

measured length. The width and thickness of the elastomer film are 44mm and 52μm, respectively. The dimensions, loading weight, and applied voltage are shown in Figure 4.1.
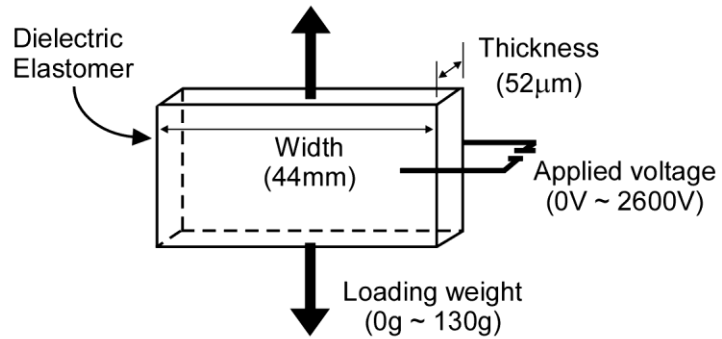
Figure 4.1. Dimensions of the DE Actuator
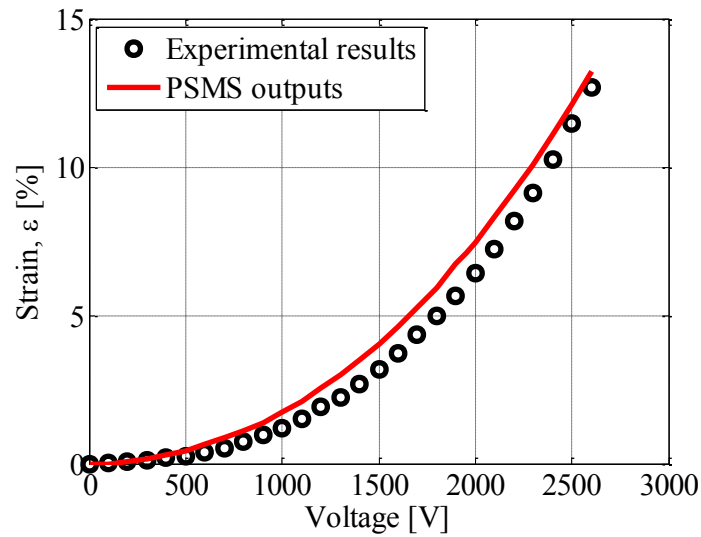
Figure 4.2. Comparison of the Engineering Strain between Experimental Data [17] and the PSMS outputs

Figure 4.2 shows the engineering strain results at an optimum weight of 55g. The PSMS outputs are plotted in a Matlab figure to compare with the experimental results. According to Kofod, a maximum strain is 12.68% at an applied weight of 55g and an applied voltage of 2600V. When a loading weight exceeds 55g, the maximum strain at 2600V is reduced [17]. The PSMS error is 4.2% at the maximum voltage. Even though the error is greater at the voltages lower than 2600V, the Ogden model of the DE actuator is only fitted to the force-strain behavior of DEs [17]. The fitting parameters of the Ogden model describe physical properties of the DE material.

Type	μ1 [kPa]	k1	μ2 [kPa]	k2	λ	α0	Δα
Silicone	596	0.859	29.6	5.46	0.716	1.657	0.0873

Table 4.1. Fitting Parameters of Ogden Model [16]
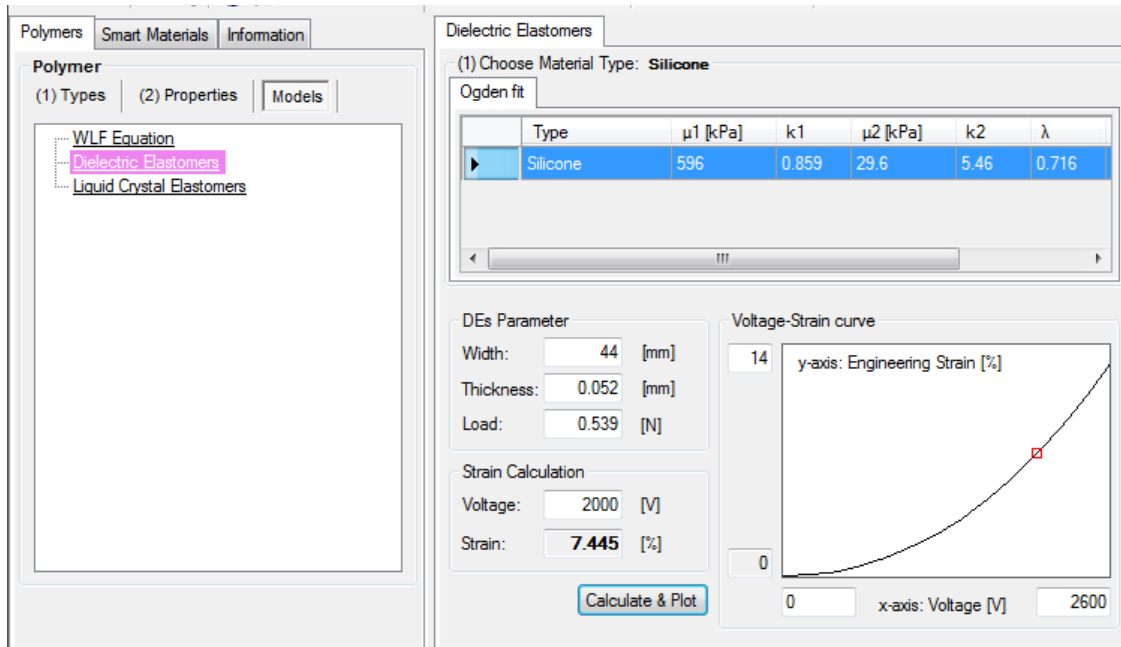
Figure 4.3. DEs Interface

The fitting parameters in Table 4.1 are compiled in the database shown in Figure 4.3. The silicone material type is chosen from the database table. The load, 0.539N in Figure 4.3 corresponds to 55 grams force. The film thickness and film width shown in Figure 4.1 are typed in the text boxes inside the "DEs parameter" group. The engineering strain is obtained from the force equilibrium consisting of the Ogden model, Maxwell force, and tensile loading, which are shown in Equations (2.2)-(2.5). The voltage-strain curve is plotted over the range between 0V and 2600V. The output strain value, 7.445% is the engineering strain value at an input voltage of 2000V.

4.1.2 Piezoelectric actuators

4.1.2.1 Bimorph actuator

Wang et al. [72] fabricated a rectangular bimorph actuator configured as a series type and mounted as a cantilever. Bending displacement and generated force are measured when a voltage is applied. The dimensions of each thin PZT ceramic plate are 40mm width, 7mm length, and 0.5mm thickness. The thickness of a metal shim serving as a center vane is 0.38mm. The PZT material type is PZT 3203HD (Motorola, Albuquerque, NM). Two PZT plates and one metal shim are bonded using epoxy resin.

Actuator tip displacement and blocking force as a function of electric field were measured using an MTI-2000 fiber-optic Fotonic sensor systems (MTI Instrument, Lathem, New York) and a force load cell (Entran PS-15, Entran Devices, Inc., Fairfield, NJ), respectively [72]. The operating frequency was 10Hz, which was much lower than

the bending resonance frequency. The fundamental harmonic bending resonance is higher than 300Hz.

As shown in Figure 4.4, the experimental tip deflection agrees well with PSMS outputs when the applied electric field is lower than 50V/mm. The difference between experimental results and PSMS outputs increases at a higher electric field. PSMS outputs show a linear function of electric field, while PZT ceramics exhibit a nonlinear electromechanical response when a high electric field is applied. Soft type PZT ceramics such as PZT 3203HD give more significant nonlinear effects than hard PZT ceramics [72]. The blocking force agrees well with PSMS outputs as shown in Figure 4.5.
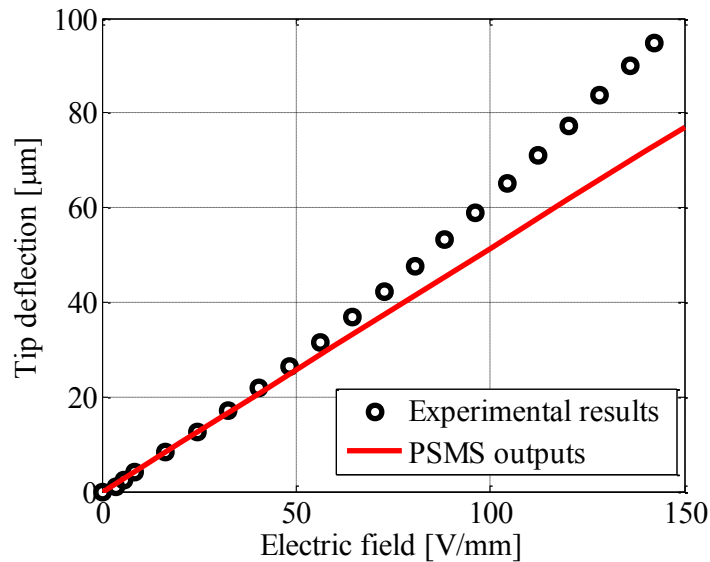
Figure 4.4. Tip Deflection of a Bimorph Actuator
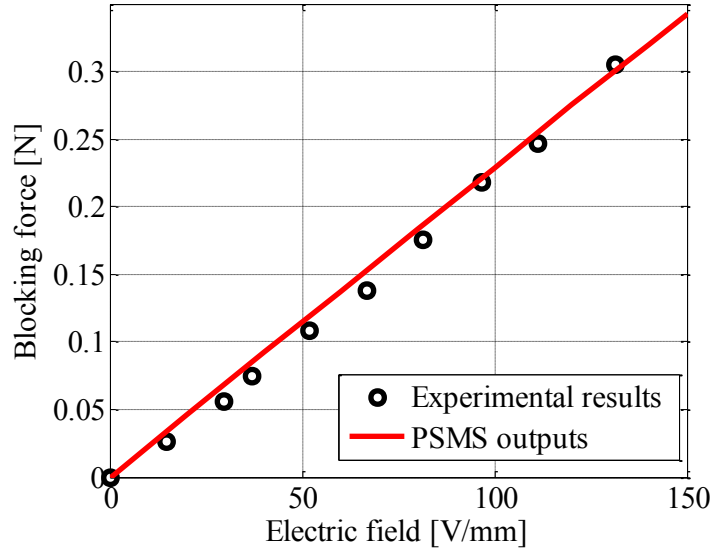
Figure 4.5. Blocking Force of a Bimorph Actuator

In Figure 4.4 and Figure 4.5, the PSMS outputs are plotted in Matlab figures. Next shows how to obtain the bimorph actuator outputs by using the PSMS. The material properties for PZT 3203HD shown in Table 4.2 are added in the database table shown in Figure 4.6.

Material Type	K33	d31 [m/V]	k31	Y11 [GPa]	tanδ	g31 [Vm/N]	Y33 [GPa]	d33 [m/V]
PZT 3203HD	3800	3.2E-10	0.43	62	0.02	0.0095	49	6.5E-10

Table 4.2. Material properties for PZT 3203HD [74]

The material properties in Table 4.2 are obtained from CTS (formerly Motorola) [74]. In Figure 4.6, the newly added material type (PZT-3203HD) is selected.

Figure 4.6 Database Including the Material Properties of PZT-3203HD

(a)

(b)

Figure 4.7 (a) Input Parameters and (b) Actuator Performance for a Bimorph Actuator

As shown in Figure 4.7a, the input parameter values are typed based on the dimensions of the bimorph actuator fabricated by Wang et al. Figure 4.7b shows the actuator performance at a driving voltage of 100V and a frequency of 10Hz.

4.1.2.2 Multilayer piezoceramic actuator

Figure 4.8 shows the configuration of a multilayer piezoceramic actuator, S-150-11C (Sinoceramics, Inc., Shanghai, China). The shape of the ceramic layer is a square of sides of 5.1mm. The characteristic values of the PZT stack actuator is given in Table 4.3.
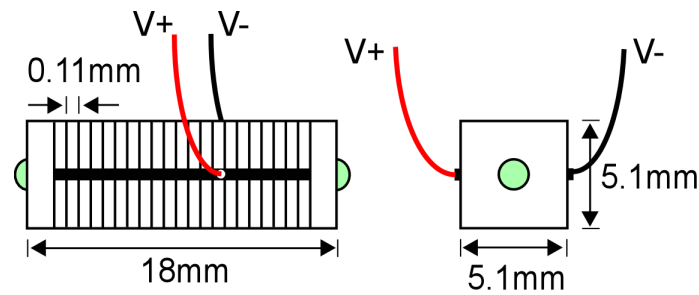
Figure 4.8. Multilayer Piezoceramic Actuator (S-150-11C) [73]

PZT stack actuator	S-150-11C [73]	PSMS
Thickness of ceramics [mm]	0.11	←
Number of ceramics	150	←
Total length [mm]	18	←
Side length [mm]	5.1	←
Driving voltage [V]	150	←
Capacitance [μF]	1.1	1.4
Deflection [μm]	18	16.88
Blocked force [N]	1000	1048.53

Table 4.3. Characteristic Values of the PZT Stacks made of PZT-5X and PSMS Results

Because the PZT stack actuator, S-150-11C is made of PZT-5X [73], the same material type PZT-5X is selected from the database table shown in Figure 4.9. The geometry values of the actuator are typed in the PSMS as shown in Figure 4.10a. The PSMS outputs such as capacitance, deflection, and blocked force are calculated at a driving voltage of 150V and displayed in Figure 4.10b as a result.

Material Properties	Input Parameters	Actuator Performance			
(1) Choose Material Type: **PZT-5X**					
Type	K33	d31	k31	Y11	
PZT-5H	3400	2.83E-10	0.4	60	
PZT-5J	2800	2.1E-10	0.34	68	
PZT-8	1000	1.05E-10	0.34	86	
PZT-5X	4500	3.2E-10	0.4	61	
PZT-4D	1280	1.45E-10	0.33	75	

Figure 4.9 Material Selection for a Multilayer Stack Actuator

Material Properties	Input Parameters	Actuator Performance
You have chosen		
Material Type: **PZT-5X**		

(2) Input Parameters:		
Actuator length (L):	5.1	[mm]
Actuator width (w):	5.1	[mm]
Actuator thickness (t):	0.11	[mm]
Actuator drive voltage (V):	150	[V]
Frequency (f):	1	[herz]
Number of layers (n):	150	
Actuator height (h):	18	[mm]

Material Properties	Input Parameters	Actuator Performanc
Performance		

Parameter	Multilayer Actuator
Capacitance [nF]	1413.16
Current [mA]	1.33
Electrical Power [mW]	199.78
Deflection [μm]	16.88
Blocked Force [N]	1048.53
Max. Mechanical Power [mW]	60.64

(a)   (b)

Figure 4.10. Program (PSMS) Result for Multilayer Stack Actuator: (a) Input Parameters and (b) Actuator Performance

The capacitance, deflection, and blocked force values from the stack actuator (S-150-11C) [73] are 1.1μF, 18μm, and 1000N, respectively. These experimental results are compared with the PSMS outputs in Table 4.3. The deflection error at a driving voltage of 150V is -6.2%.

Figure 4.11 shows the displacement comparison between experimental results [73] and the PSMS outputs plotted over the voltage range from 0V to 150V. The PSMS provides similar output values.
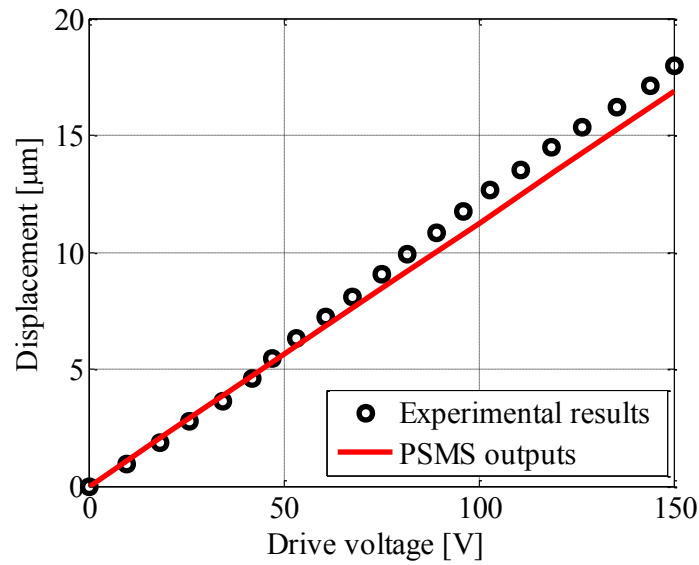
Figure 4.11. Displacement of a Multilayer Piezoceramic Actuator

4.1.3 SMA wire application

A shape-memory alloy wire can be utilized to make the metal reinforcing strap between the tread band and the carcass of a vehicle tire. Zero-degree metal reinforcements with SMA wire are used to avoid the problems of flatspotting and centrifugal expansion in a tire [75]. The austenite start and finish temperature ranges given in the patent [75] are between about 40 and 90°C and between about 60 and 120°C, respectively. The maximum stress at the austenite finish temperature is between 400 and 600MPa. It is assumed that the change in temperature is zero and the material is initially in the austenitic state. We set the temperature and maximum stress as 90°C for temperature and 500MPa for maximum stress. Table 4.4 shows the different compositions of SMA material and resulting strain values calculated from the program. The austenite finish temperatures (A_f) are all below 90°C.

Compostion	$Ti_{50}Ni_{50}$	$Ti_{50}Ni_{40}Cu_{10}$	$Ti_{48.5}Pd_{30}Ni_{21.5}$
M_f [°C]	15	20.9	-2
M_s [°C]	55	41.4	40.6
A_s [°C]	80	52.7	36.8
A_f [°C]	89	66.6	61.4
C_A [MPa/°C]	7	10	5
C_M [MPa/°C]	7	10	5
E_A [GPa]	70	50	15
E_M [GPa]	30	25	25
ε_{max}	6%	5%	3%
Strain(M→A)	7.67%	7%	5%

Table 4.4. Three Different SMA Material Properties and Resulting Strain Values at 90°C and 500MPa
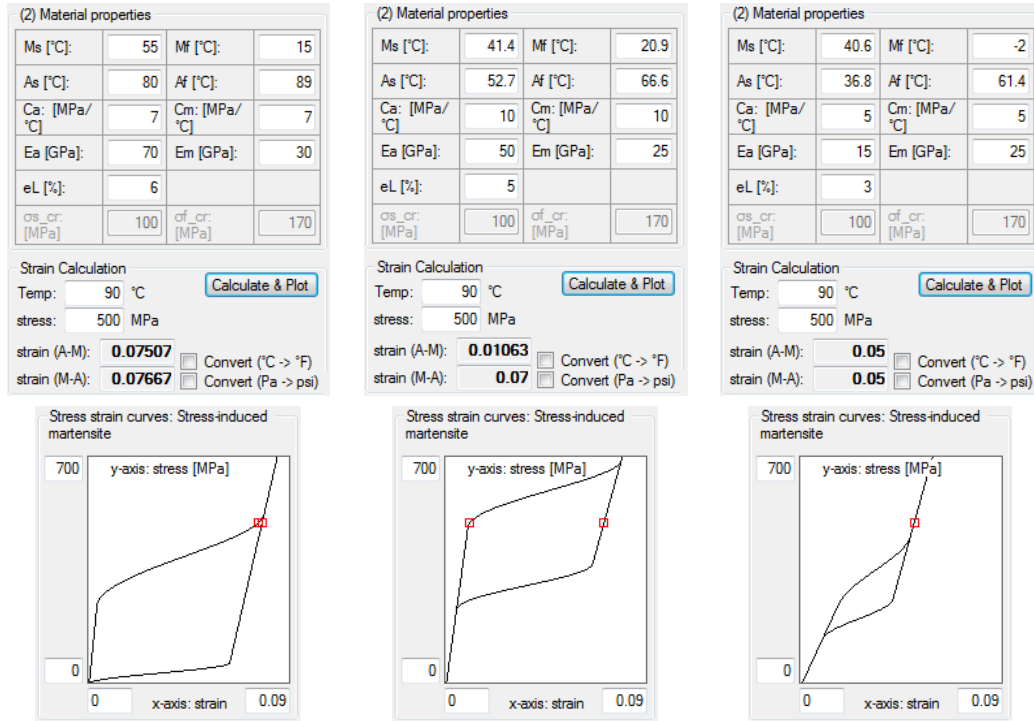
Figure 4.12. SMA Round Wire Strain Calculation Program (SMA Materials, from Left to Right: Ti50Ni50, Ti50Ni40Cu10, and Ti48.5Pd30Ni21.5)

Figure 4.12 shows the program to calculate strain values in three different SMA materials shown in Table 4.4. Liang and Rogers' model is selected to plot the stress-strain curves. Ti50Ni50 produces the largest strain value (stress induced martensite → austenite), 7.67% as compared with two other materials. As a result, the software results would suggest that Ti50Ni50 material can be considered first considered to improve the rigidity of the belt so that flatspotting and centrifugal expansion can be avoided.

4.1.4 Thermoelectric power generator application

A thermoelectric module provides electrical energy to a sensing module by converting heat conducted from a tire [76]. A thermoelectric generator is integrated

66

within the tire pressure monitoring (TPM) sensor housing. A typical TPM sensor consumes about 3V and 10mA for when transmitting, so the required power is 0.03 Watts. Based on tire performance data, we assume that the hot side and the cold side temperatures are 90°C and 50°C, respectively. After selecting a TE module type, the maximum output power of one module is calculated and then the minimum number of modules is determined to meet the power requirement (see Figure 4.13a). The maximum power of one module is 0.151 Watts when a 31-Couple and 9-Ampere Ferrotec module is selected. The number of couples and current in each TE module can be customized as shown in Figure 4.13b. Instead of using a 31-Couple and 9-Ampere TE module, a 16-Couple and 9-Ampere TE module can be considered because the customized module produces 0.078 Watts maximum output power, which is enough to meet the power requirement for the transmission mode of a TPM sensor.

(a)   (b)
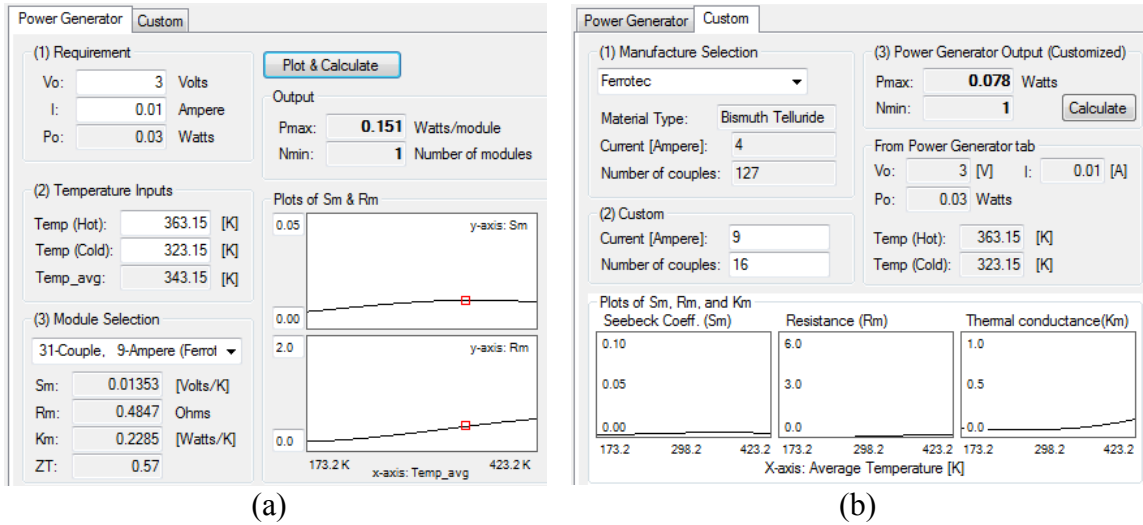
Figure 4.13. (a) TE Power Generator and (b) Customized TE Module

4.2 Material and Performance Chart

This section shows material and performance charts which include values or plots for multiple material types.
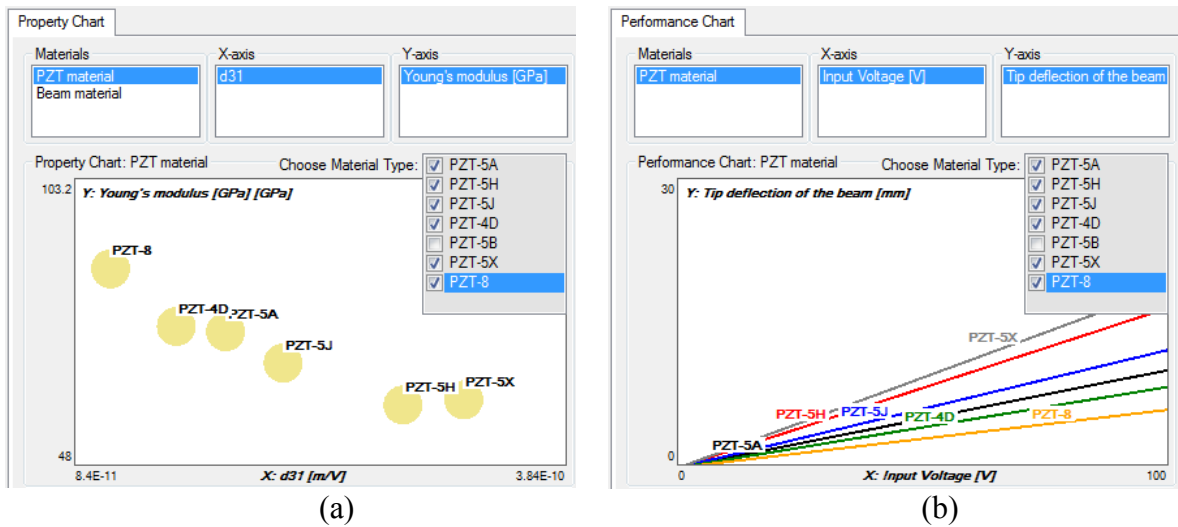
Figure 4.14. (a) Material Property Chart and (b) Performance Chart

Figure 4.14a shows a material property data chart for PZT materials. This chart helps users to compare material properties visually. Figure 4.14b shows the performance data for selected material types. This is an example for a rainbow/thunder actuator. The tip deflection of the actuator beam is plotted over input voltages. These two charts are useful to determine which material is the best for a given design goal.

Chapter 5 : Light-Induced Deformation of Liquid Crystal Elastomers

A modified bending model based on a gradient model is proposed in order to further develop a viscoelastic photo-strain model, which is presented with a time-explicit expression for the light-strain-temperature-time relationship. This time dependence is needed for dynamic applications.

5.1 Introduction

Liquid crystals (LCs) exhibit properties between a liquid and a solid crystal. LCs are categorized into four different phases depending on the degree of positional or orientational ordering as follows: isotropic, nematic, smectic, and crystalline. Nematic LCs have long-range molecular orientational order, but no positional order. In this chapter, nematic side-chain liquid crystal elastomers are discussed and used for light-induced deformation.

Liquid crystal polymers (LCPs) deform when constituent liquid molecules orientate. LCPs can be divided into three different types depending on the attachment of mesogens and backbone polymer chains. They are main-chain, side-on side-chain, and end-on side-chain LCPs. For side-on side-chain LCPs, mesogens are attached to the backbone as side groups. LCPs become anisotropic fluids when temperature reaches above the glass transition temperature.

Liquid crystal elastomers (LCEs) are composed of cross-linked LCPs and possess the elastic properties of rubbers due to the cross-linked formation. LCEs have the ability to maintain their shapes and to return to their original configurations.

Figure 5.1 illustrates the photo-responsive bending deformation of liquid crystal elastomer film clamped on one side. The thin photochromic LCE film is illuminated by UV light perpendicularly and uniformly. The illuminated UV light penetrates up to a certain depth into the film depending on the light intensity and material density. The photo-responsive azo dyes absorb UV light and transform from rod-like *trans* isomers into bent *cis* ones. This process is called a photo-isomerization. Due to the transformed bent *cis* isomers, the beam contracts along the x direction indicated in Figure 5.1. The photo-strain is the maximum on the top surface and exponentially decreases through the thickness of the LCE film.
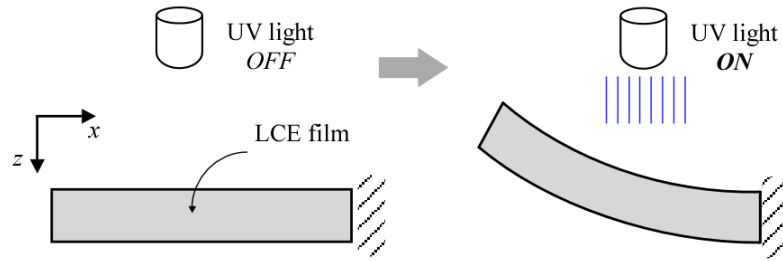
Figure 5.1. LCE Film Bending when UV Light is on

The light-induced contraction is inhomogeneous because the light intensity decays exponentially through the thickness [57]. Therefore, the contraction varies along the z direction and bending occurs due to the strain variation.

5.2 Gradient Bending Model

The constitutive relation of the liquid crystal elastomers is introduced by considering the light and temperature effect. Strain and Young's modulus is inhomogeneous to light and the effect of light is introduced as an effective optical bending moment.

Jin et al. [56] introduced a gradient bending model by deriving the opto-mechanical constitutive relation from the photo-isomerization process and the nematic-isotropic phase transition. They developed the gradient bending model of LCEs using Hamilton's principle and they have produced equations that highlight the bending deflection curve.

A photo strain is expressed with a stress free deformation λ_m written in terms of the number fraction of the *cis* density ϕ and temperature. λ_m is given by [56]

$$\lambda_m(I) = \left(1 + \alpha\left(T_{ni}^0 - T - \beta\phi(I)\right)^{\xi}\right) \Big/ \left(1 + \alpha\left(T_{ni}^0 - T\right)^{\xi}\right) \tag{5.1}$$

where I is light intensity, T_{ni}^0 is nematic-isotropic phase transition temperature before illumination, and T is room temperature. α, β, and ξ are positive constants.

The Young's modulus E and the stress-free strain ε_m are expressed using λ_m as follows [56].

$$E(I) = \mu\left(\lambda_m(I) + \frac{2}{\lambda_m^2(I)}\right) \quad \text{and}$$

$$\varepsilon_m(I) = \left(\lambda_m(I) - \frac{1}{\lambda_m^2(I)}\right) \Big/ \left(\lambda_m(I) + \frac{2}{\lambda_m^2(I)}\right) \tag{5.2}$$

where μ is an effective shear modulus. E and ε_m both depend on the light intensity and are inhomogeneous through the film thickness.

71

The gradient bending moment term M_{eff} is written by [56]

$$M_{eff} = w \int_0^h E(I) \left[\varepsilon_m(I) - h \frac{\int_0^h E(I) \varepsilon_m(I) dz}{\int_0^h E(I) dz} \right] z dz \qquad (5.3)$$

The blocked force $3M_{eff}/2L$ is calculated under the condition of uniform illumination. In previous research, the blocked force was measured by other researchers [58].

Jin et al. show similar agreement by comparing the gradient bending model's behavior with a blocked force from experimental results given by Camacho-Lopez et al. [58]. Jin et al. simulated the gradient model by choosing $\theta = 0.88$, $h/d = 4$, $i_{0r} = 3$, $L/h = 10$, $\mu = 3.1 \times 10^6 \text{N/m}^2$, $w = 5\text{mm}$, and $h = 0.32\text{mm}$. The UV light is exposed to a LCE film uniformly during 60ms, and then the UV light is turned off. Camacho-Lopez et al. measured the blocked force of a dye-doped LCE sample by using an ultra-high sensitivity Entran force sensor. In the gradient model, the stress-free deformation term λ_m was validated by a similar comparison.

5.3 Simplified Bending Model

The gradient model by Jin et al. is difficult to incorporate for system-based implementation, i.e., time, frequency, because in this model is time implicit. LCE materials will be used for real time application. Thus a time-explicit model needs to be developed. In order to develop a time-explicit model, the gradient bending model is modified as a simplified bending model in this section. In the next section 5.4, the

simplified bending model is expressed in a viscoelastic photo-strain model and the final strain model becomes time-explicit.

Strain and Young's modulus terms, which are expressed using the deformation term, are used in the simplified bending model and to calculate LCE film deflection in the software. The bending moment expression in Equation (5.3) is simplified by changing the *x-z* coordinate as shown in Figure 5.2. The origin of the *x-z* coordinate is relocated on the center thickness with the *z* axis pointed upward. The multiplication of strain and Young's modulus is integrated throughout the thickness. The simplified bending moment is given in Equation (5.4) [77].
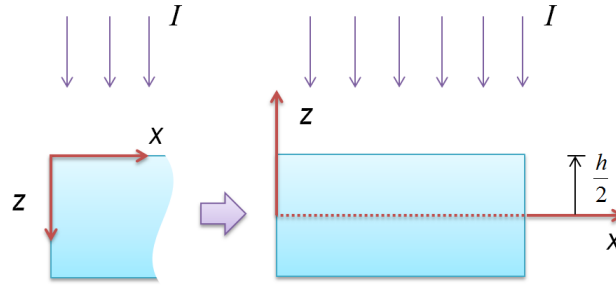
Figure 5.2. Change of the *x-z* Coordinate from the Gradient Bending Model to the Simplified Bending Model

$$M_\Lambda = w\int_{h/2}^{-h/2} E(I)\varepsilon_m(I)zdz = \mu w\int_{h/2}^{-h/2}\left(\lambda_m(I)-\frac{1}{\lambda_m^2(I)}\right)\left(\frac{h}{2}-z\right)dz \qquad (5.4)$$

As shown in Figure 5.3, the blocked force $3M_\Lambda/2L$ is plotted to compare with the experimental results [58]. The UV light is turned on at 0msec and turned off at 60msec. The same parameter values used by Jin et al. [56] are applied to compare the experimental results.
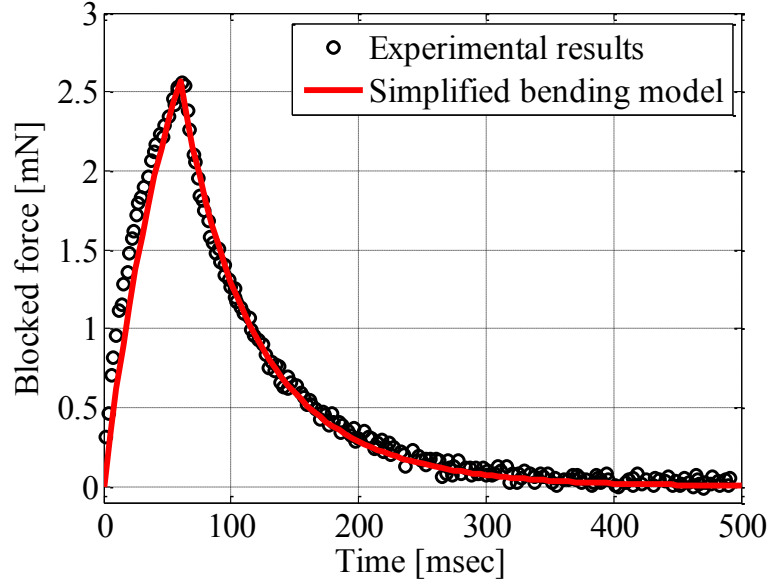
Figure 5.3. Comparison between Experimental Results [58] and Blocked Forces using Simplified Bending Model

The simplified bending model shows good agreement with the experimental results. Using this model, the deflection along the LCE film is derived.

The curvature of the bending is

$$\kappa = \frac{\partial^2 w}{\partial x^2} \quad \rightarrow \quad \frac{M_\Lambda}{(YI)_{total}} = \frac{\partial^2 w}{\partial x^2} \tag{5.5}$$

The deflection along the LCE film length is obtained by integrating and applying the boundary condition that the right end of the film is fixed.

$$w = \frac{1}{2} \frac{M_\Lambda}{(YI)_{total}} (x - L)^2 \tag{5.6}$$

Equation (5.6) and $3M_\Lambda/2L$ are incorporated into the tool to calculate a tip deflection and a blocked force. Figure 5.4 shows the film deflection along the length and maximum tip deflection over penetration depth. Figure 5.5 shows the blocked force.

74

Figure 5.4 LCE Film Deflection and Deflection vs. Penetration Depth
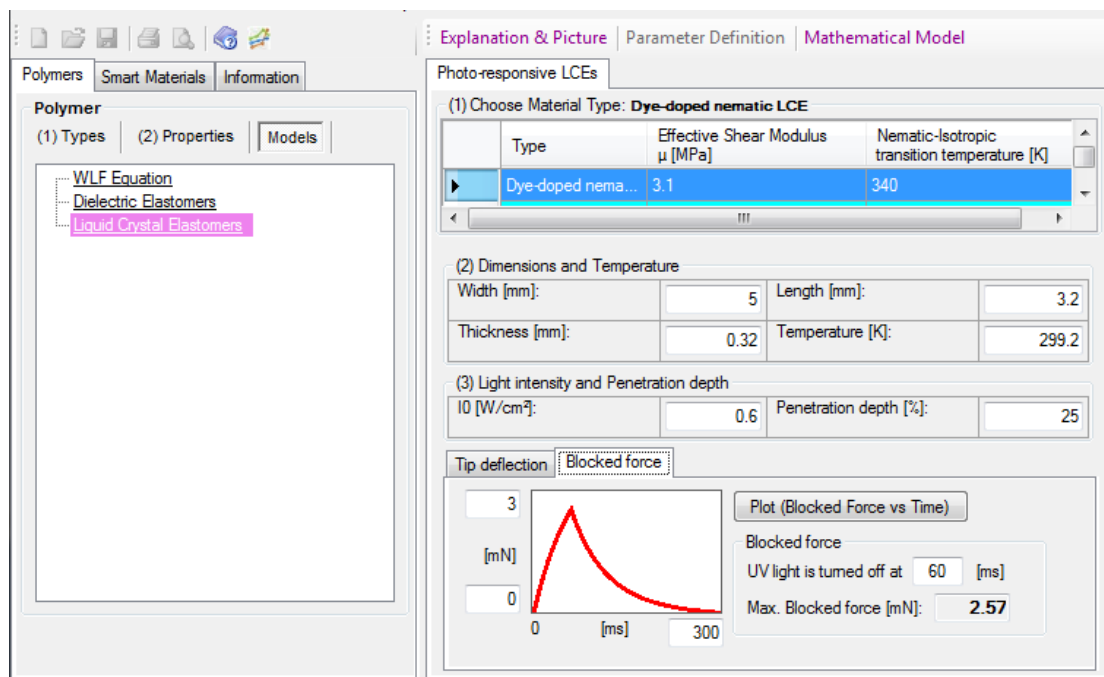
Figure 5.5 Blocked Force

5.4 Viscoelastic Photo-Strain Model

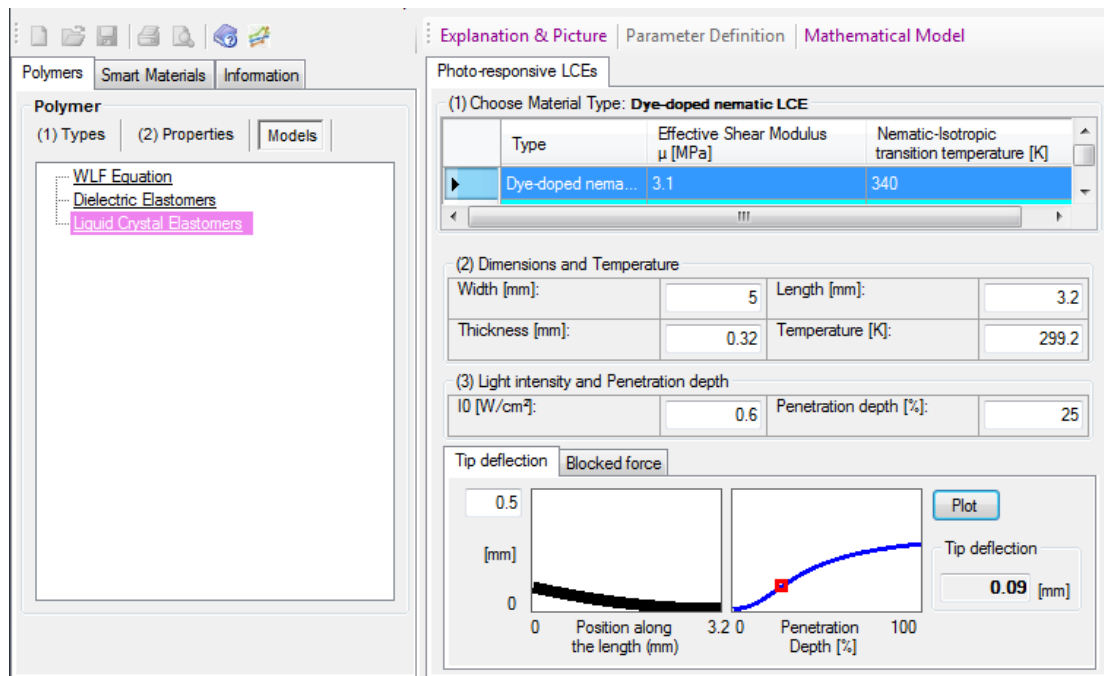LCEs experience a time-dependent increase in strain when subjected to a constant light exposure. When applied light is removed, the strain in LCEs decreases exponentially to zero strain. This phenomenon is similar to viscoelastic creep. Thus, viscoelastic behavior in LCEs can be expressed using the Voigt-Kelvin model, which consists of a damper and a spring together in parallel. Based on this viscoelastic model, the bending model of LCEs is further developed to describe the light-strain-temperature-time relationship. Since the strain in LCEs is stress-free and induced by light only, the stress term in the viscoelastic expression is replaced with a light term later. Figure 5.6 shows the Voigt-Kelvin model with two elements: a spring and a damper.

Figure 5.6. Voigt-Kelvin Model

In Figure 5.6, E is a spring constant and η is a viscous resistance coefficient. The total stress, $\sigma(t)$ is the summation of the stresses in the two elements as shown in Equation (5.7).

$$\sigma(t) = E\varepsilon(t) + \eta \frac{d\varepsilon(t)}{dt} \tag{5.7}$$

In creep response, the applied stress $\sigma(t)$ is a constant value σ_0 with respect to time. Thus $\sigma(t) = \sigma_0$. Equation (5.7) is written by
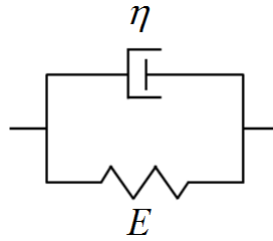
$$\frac{d\varepsilon(t)}{dt} + \frac{E}{\eta}\varepsilon(t) = \frac{\sigma_0}{\eta} \tag{5.8}$$

Then, the strain term $\varepsilon(t)$ is obtained from a solution of the linear differential equation shown in Equation (5.8).

$$\varepsilon(t) = \frac{\sigma_0}{E}\left[1 - \exp\left(-t/\tau_r\right)\right] \tag{5.9}$$

where $\tau_r = \eta/E$. τ_r is retardation time.
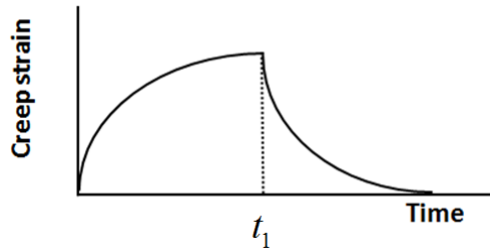
Figure 5.7. Creep Strain vs Time (Viscoelastic Behavior when a Stretching Force is Present and then Removed at t_1)

Since the strain in LCEs varies depending on light intensity (I_0), depth (z) through the thickness, and time (t), the strain term from Equation (5.9) is written as a function of I_0, z, and t.

$$\varepsilon(I_0, z, t) = \frac{\sigma_0(I_0, z, t)}{E}\left[1 - \exp\left(-t/\tau_r\right)\right] \tag{5.10}$$

77

Since LCE strain is induced by a light source, the constant stress σ_0 needs to be replaced to a term expressed with a light intensity. The general expression of a light-induced strain is given by

$$\varepsilon_{photo} = cI_0 exp\left(-z/d\right)$$ (5.11)

where c is constant and d is light penetration depth. The light-induced strain equation is used to replace the stress-strain relationship shown in Equation (5.10). Equation (5.11) is a steady state value and time independent. Thus we consider Equation (5.10) as time approaches infinity in order to compare both equations. Then, Equation (5.10) becomes

$$\varepsilon\left(I,z,t_\infty\right) = \frac{\sigma_0\left(I,z,t_\infty\right)}{E}\left[1-exp\left(-t_\infty/\tau_r\right)\right] = \frac{\sigma_0\left(I,z,t_\infty\right)}{E}$$ (5.12)

Since ε (I,z,t_∞) is assumed to be the same as ε_{photo}, σ_0 can be replaced with $cEI_0exp(-z/d)$ as shown in Equation (5.13).

$$\frac{\sigma_0\left(I,z,t_\infty\right)}{E} = cI_0 \exp\left(-z/d\right) \quad \rightarrow \quad \sigma_0\left(I,z,t_\infty\right) = cEI_0 \exp\left(-z/d\right)$$ (5.13)

Then, viscoelastic photo strain term is written as

$$\varepsilon\left(I_0,z,t\right) = cI_0 exp\left(-z/d\right)\left[1-exp\left(-t/\tau_{r_{ON}}\right)\right]$$ (5.14)

When the UV light is turned off, the strain term becomes

$$\varepsilon\left(I_0,z,t\right) = cI_0 exp\left(-z/d\right)\left[exp\left(-t/\tau_{r_{OFF}}\right)\right]$$ (5.15)

Time is explicit and shown in the strain model. The strain varies with time and asymptotically approaches a steady value.

The values of c and τ_r are mapped to incorporate a temperature change. Here c is described as a function of temperature to express the steady values of strain. Each

retardation time τ_r in Equations (5.14) and (5.15) is mapped to incorporate a temperature change. This value is written as a function of temperature.

Strain values at steady state vary with temperature. In Figure 5.8, the circle markers are the data obtained from the gradient model and the solid line is the fitting curve. The steady state strains are values at 25% penetration depth.
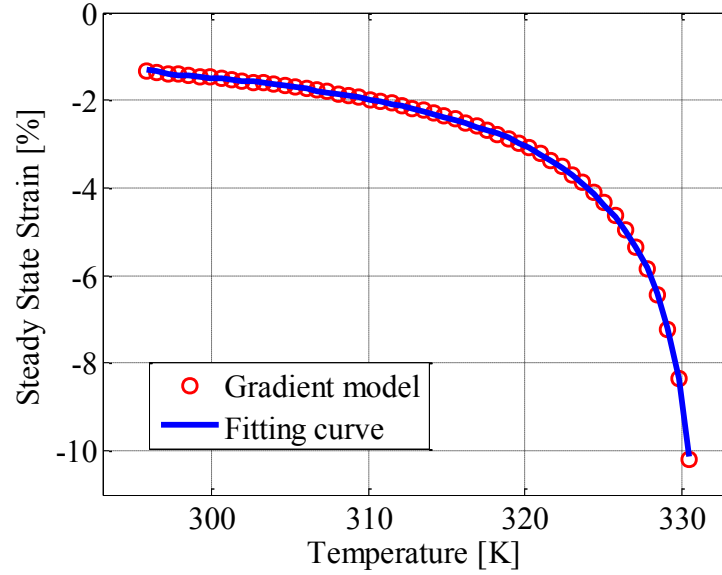
Figure 5.8. Steady State Strain vs. Temperature

The fitting curve is obtained by using a Gaussian curve fit in Matlab. The fitting curve function C_{fit} is

$$C_{fit}(T) = \sum_{n=1}^{7} a_n \exp\left(-\left((T - p_n)/q_n\right)^2\right)$$

(5.16)

where T is temperature. a, p, and q's are coefficients. The value of c given in Equation (5.14) is now described as a function of temperature to express the steady values of strain.

$$c(T) = \frac{C_{fit}(T)}{i_0} \qquad (5.17)$$

The viscoelastic photo strain term is rewritten using the temperature dependant $c(T)$.

$$\varepsilon\left(I_0, T, z, t\right) = \begin{cases} c(T)I_0 exp\left(-z/d\right)\left[1 - exp\left(-t/\tau_{r_{ON}}\right)\right] & \text{when light is turned on} \\ c(T)I_0 exp\left(-z/d\right)\left[exp\left(-t/\tau_{r_{OFF}}\right)\right] & \text{when light is turned off} \end{cases} \qquad (5.18)$$

Figure 5.9 shows two transient curves when light is turned on and off. Retardation time is calculated for each case when light is on and off. The strain value is on the surface of the LCEs.
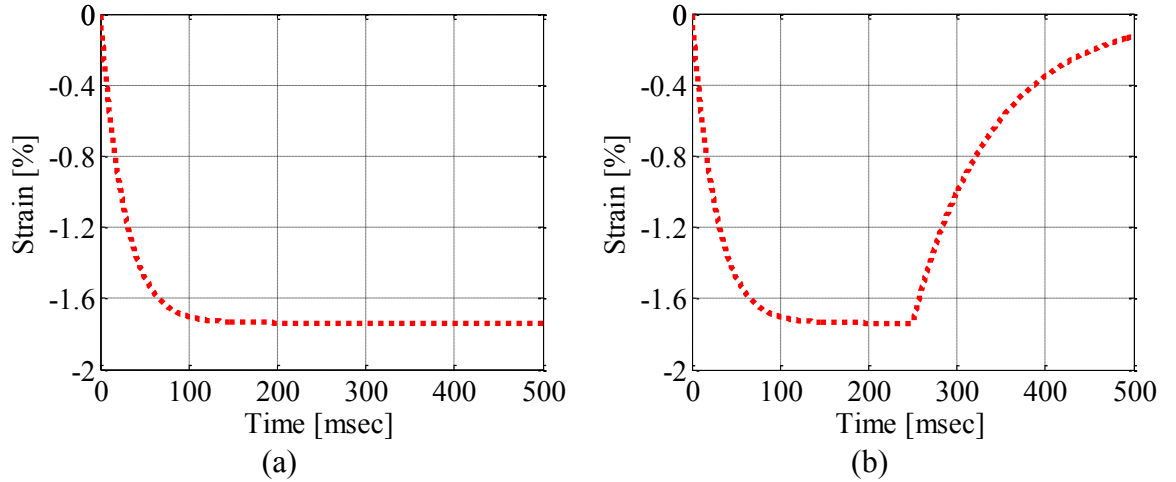
Figure 5.9. Strain vs. Time Plots obtained from the Gradient Model: (a) UV Light is turned on and (b) UV Light is turned off at 250 msec

In Figure 5.9a-b, the dotted line is plotted from the strain equation of the gradient model. When light is on, 10% of the steady state value occurs at 2.875ms and 90% of it happens at 60ms. Thus, the retardation time is 0.01(60ms-2.875ms)/ln9 and is equal to 0.26ms. In the same manner, the retardation time in Figure 5.9b is 0.95ms.

Figure 5.10 shows steady state strain values of the viscoelastic strain model given in Equation (5.18) and the gradient model at three different temperatures.
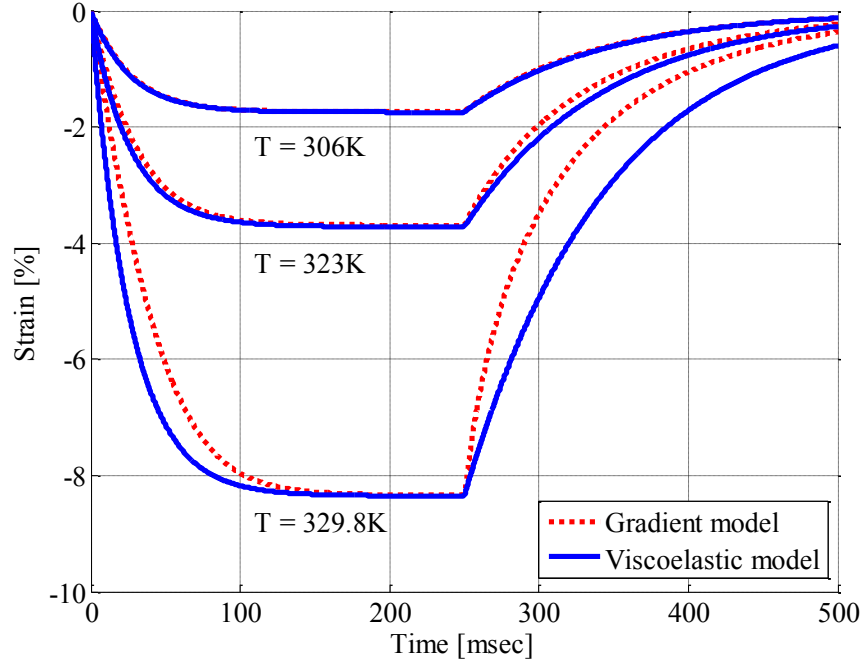
Figure 5.10. Strain vs. Time at different Temperatures (with fixed Retardation Time)

The dotted line is strain obtained from the gradient model and the solid line indicates the viscoelastic model with temperature dependant c term. The steady state strain values match well. However, retardation time values are different over temperature change. Each retardation time τ_r needs to be mapped to incorporate a temperature change.

Now the retardation time is written as a function of temperature.

$$\tau_r(T) = \sum_{n=1}^{7} a_n \exp\left(-\left((T - p_n)/q_n\right)^2\right) \tag{5.19}$$

where T is temperature. a, p, and q's are coefficients.

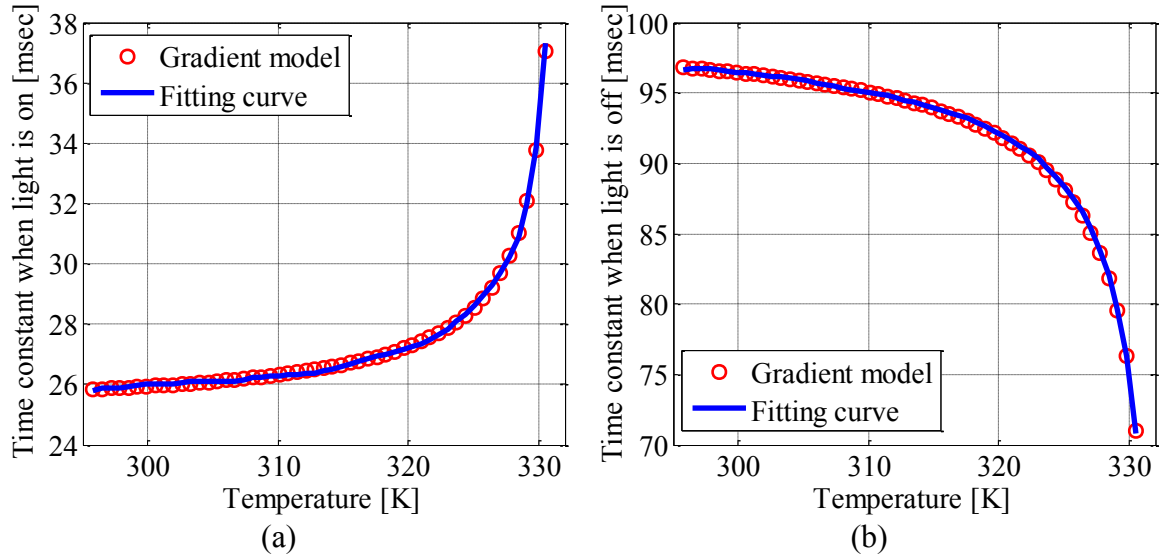Figure 5.11. Curve Fitting for Retardation Time: (a) when UV Light is on and (b) when UV Light is off
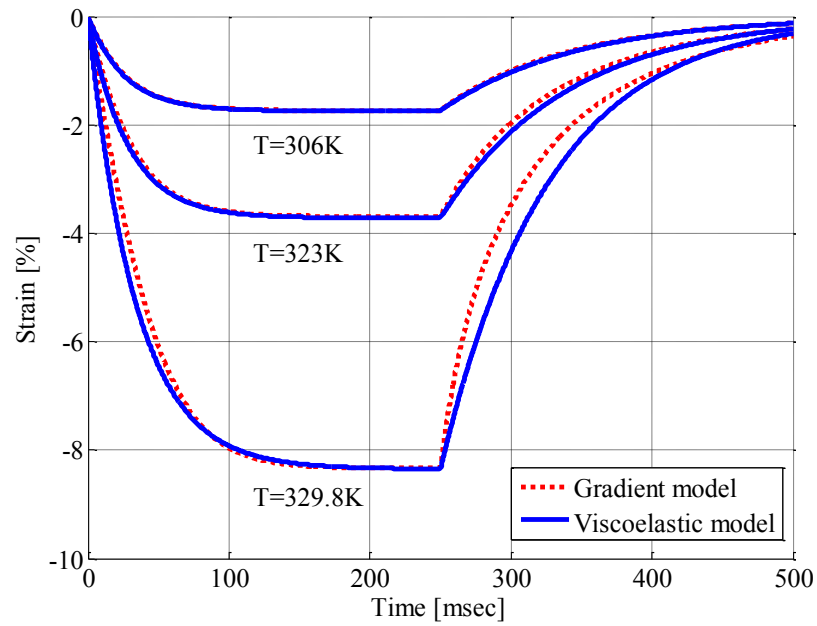

Figure 5.12. Strain vs. Time at Different Temperatures (with Variable Retardation Time)

In Figure 5.11a-b, the solid line is the curve fitting plot and the circle marks are the data obtained from the gradient model.

The dotted line in Figure 5.12 is data from the gradient model and the solid line shows the viscoelastic model results with a variable retardation time. Strain vs. time curves are plotted at three different temperatures. The c value and retardation time τ_r are both written as a function of temperature.

Temperature dependent functions ($c(T)$ and $\tau_r(T)$) in the viscoelastic photo-strain model are mapped to represent the temperature effect in the gradient model. However, the current mapping functions are only good for strain at the top surface of an LCE film, because they are mapped for only that depth ($y=h/2$). With only temperature dependant $c(T)$ and $\tau_r(T)$, the strain term is written as

$$\varepsilon\left(I_0,T,z,t\right)=\left[c(T)\cdot I_0 exp\left(-(h/2-z)/d\right)\right]\cdot\left[1-exp\left(-t/\tau_{r_{ON}}(T)\right)\right] \qquad (5.20)$$

Equation (5.20) is plotted at three different z values as shown in Figure 5.13 and compared with strain values from the gradient model. The temperature, T is 325K.
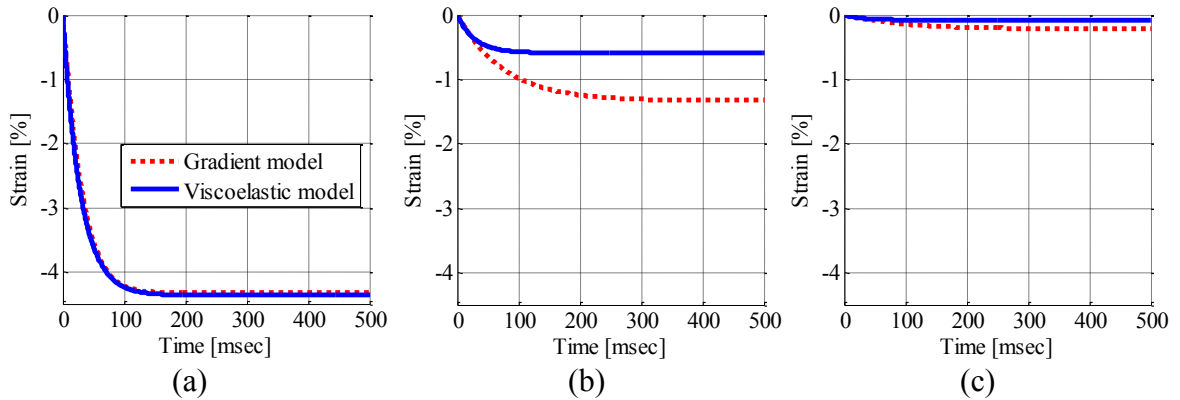

Figure 5.13. Viscoelastic photo-strain with $c(T)$ and $\tau_r(T)$: (a) $z=h/2$, (b) $z=0$, and (c) $z=-h/2$

When z values change, the steady state values do not match with the gradient model as shown in Figure 5.13. In order to take into account z variations, d term in Equation (5.20) is replaced with $\varepsilon_s(z)+d$.

$$\varepsilon(I_0,T,z,t)=\left[c(T)\cdot I_0 exp\left(-(h/2-z)/(\varepsilon_s(z)+d)\right)\right]\cdot\left[1-exp\left(-t/\tau_{r_{ON}}(T)\right)\right] \qquad (5.21)$$

In Figure 5.14, the modified strain term is plotted at three different z values again. The steady state values match with the gradient model.
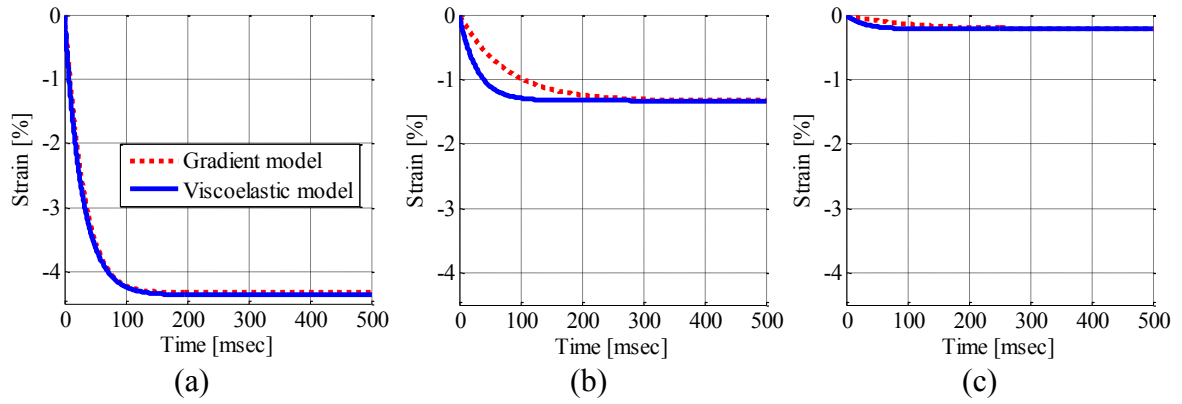
Figure 5.14. Viscoelastic photo-strain with $c(T)$, $\varepsilon_s(z)$ and $\tau_r(T)$: (a) $z=h/2$, (b) $z=0$, and (c) $z=-h/2$

The retardation times are modified by considering variations in the z axis.

$$\varepsilon(I_0,T,z,t)=\left[c(T)\cdot I_0 exp\left(-(h/2-z)/(\varepsilon_s(z)+d)\right)\right]\cdot\left[1-exp\left(-t/\tau_{r_{ON}}(T,z)\right)\right] \qquad (5.22)$$

Equation (5.22) is plotted in Figure 5.15 and matches well with the gradient model. This viscoelastic photo-strain model is time-explicit.
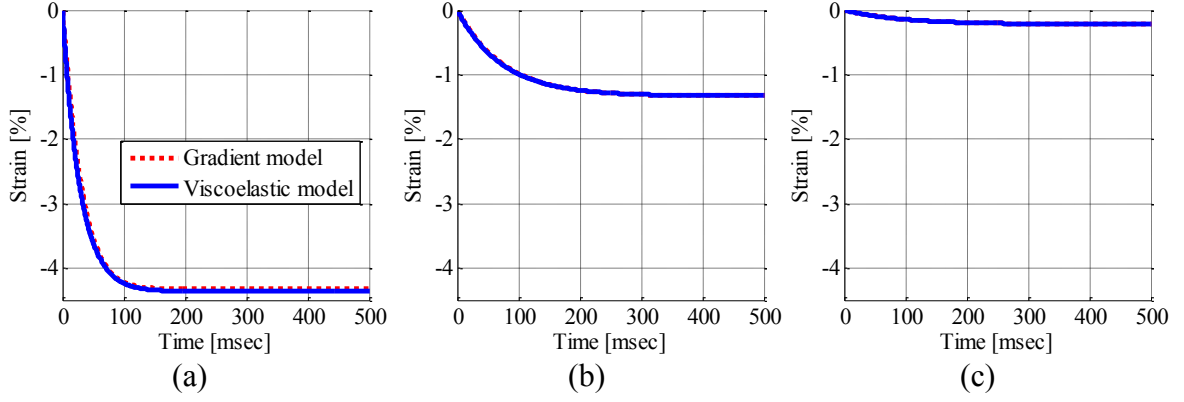
Figure 5.15. Viscoelastic photo-strain with $c(T)$, $\varepsilon_s(z)$ and $\tau_r(T,z)$: (a) $z=h/2$, (b) $z=0$, and (c) $z=-h/2$

Time constants $\tau_{r_{ON}}(T,z)$ and $\tau_{r_{OFF}}(T,z)$ are dependent on temperature and depth. They are plotted in Figure 5.16 and Figure 5.17.
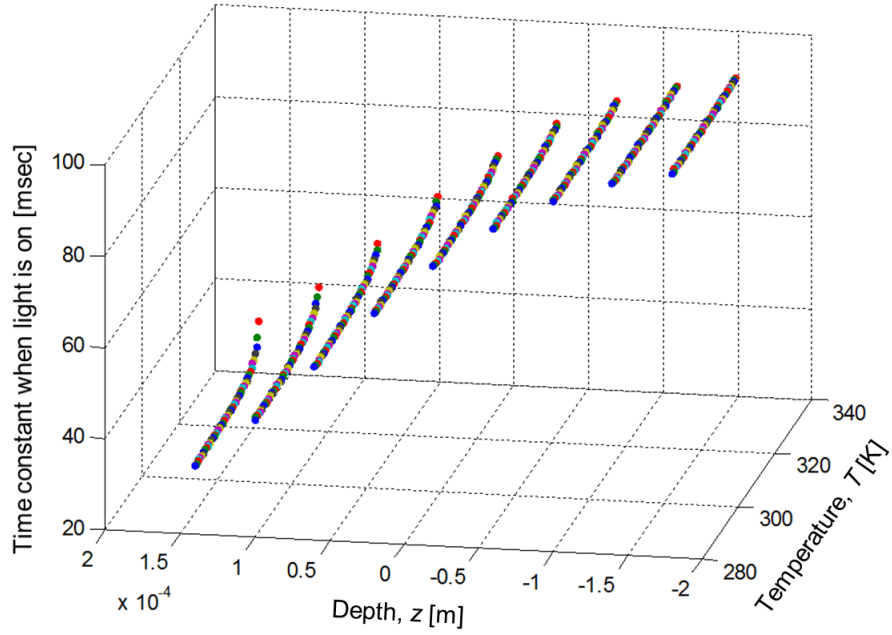
Figure 5.16. Time constant when light is on: $\tau_{r_{ON}}(T,z)$
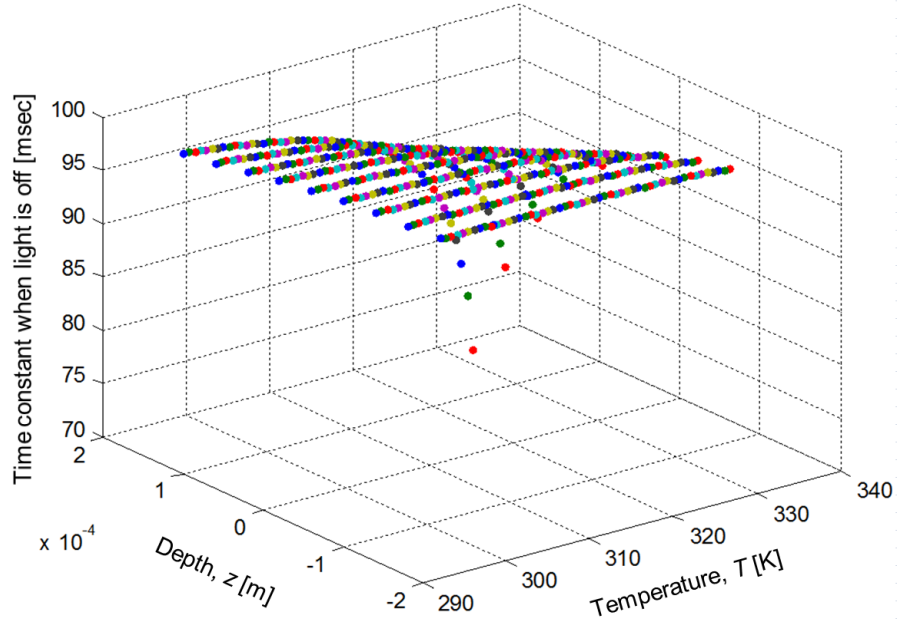
Figure 5.17. Time constant when light is on: $\tau_{r_{OFF}}(T,z)$

Steady state strain, $\varepsilon_s(T,z)$ varies depending on temperature change. $\varepsilon_s(T,z)$ is plotted in Figure 5.18.
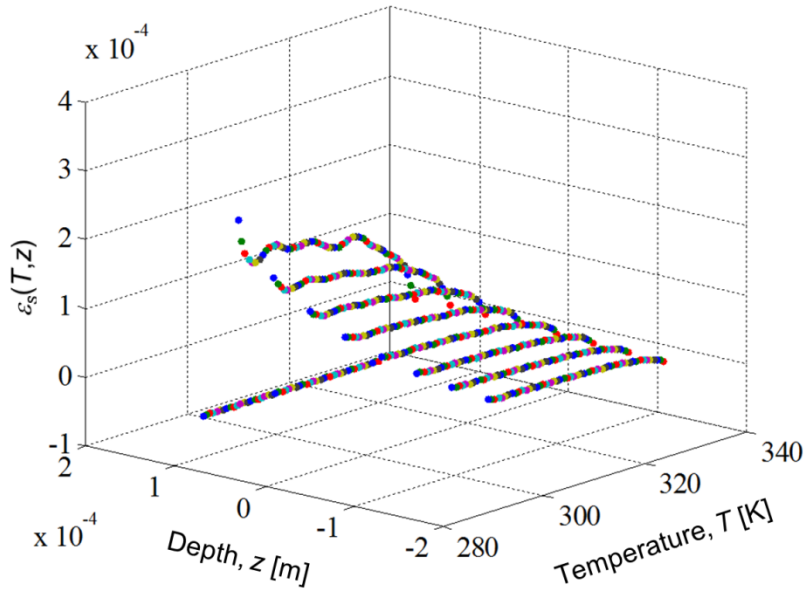
Figure 5.18. Steady state strain, $\varepsilon_s(T,z)$

86

Figure 5.16, Figure 5.17, and Figure 5.18 are fitted using a polynomial surface of degree 6 in *x*-axis and degree 6 in *y*-axis. The fitted surface is a function of temperature and depth. Equation (5.22) is rewritten with $\varepsilon_s(T,z)$ term.

$$\varepsilon(I_0,T,z,t) = \left[c(T)\cdot I_0 exp\left(-(h/2-z)/(\varepsilon_s(T,z)+d)\right)\right]\cdot\left[1-exp\left(-t/\tau_{r_{ON}}(T,z)\right)\right] \qquad (5.23)$$

When light off, Equation (5.23) becomes

$$\varepsilon(I_0,T,z,t) = \left[c(T)\cdot I_0 exp\left(-(h/2-z)/(\varepsilon_s(T,z)+d)\right)\right]\cdot\left[exp\left(-t/\tau_{r_{OFF}}(T,z)\right)\right] \qquad (5.24)$$

Equation (5.23) and (5.24) are used to plot blocked forces at different temperatures as shown in Figure 5.19. The gradient model and viscoelastic photo-strain model match well. Figure 5.19a-c shows blocked forces of gradient and viscoelastic models with varying Young's modulus. Young's modulus shown in Equation (5.2) changes up to 0.9 % when penetration depth changes from 0% to 100%. Figure 5.19d-f shows blocked forces at constant Young's modulus. When Young's modulus is assumed as constant, the bending moment term shown in (5.4) is simplified.

$$M(I_0,T,z,t) = wE\int_{h/2}^{-h/2}\varepsilon(I_0,T,z,t)\left(\frac{h}{2}-z\right)dz \qquad (5.25)$$
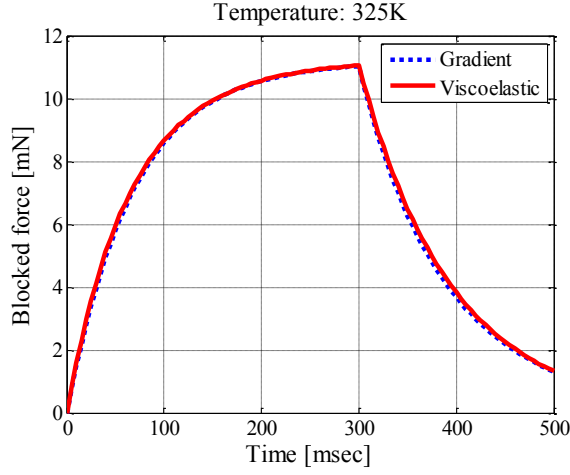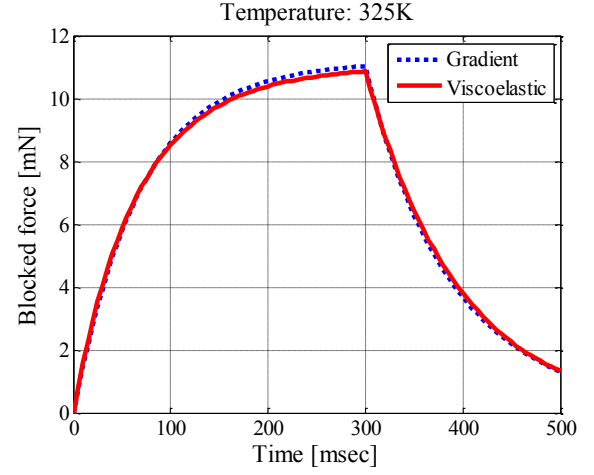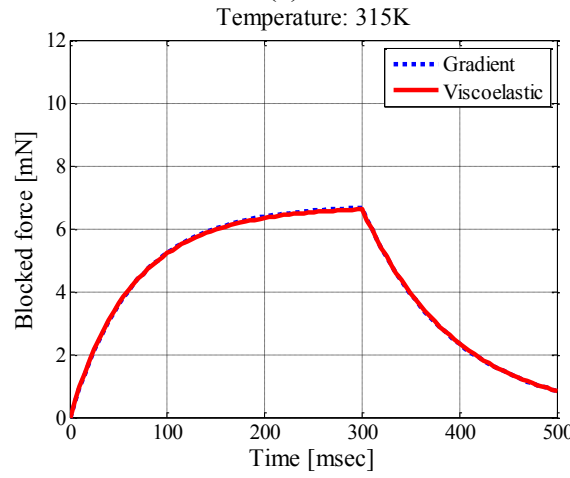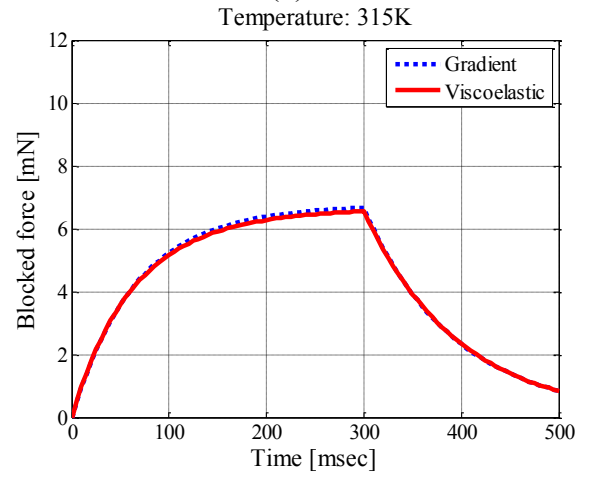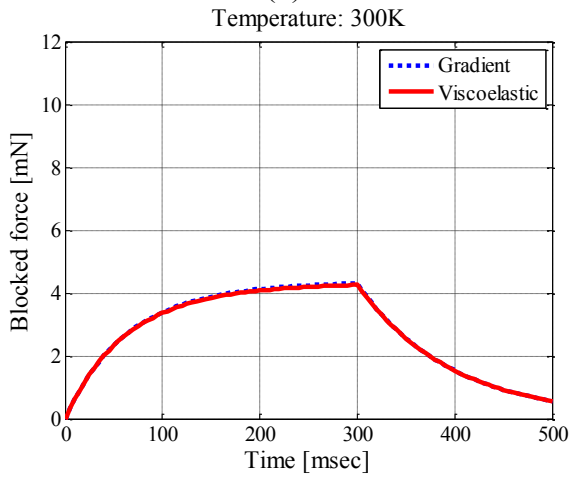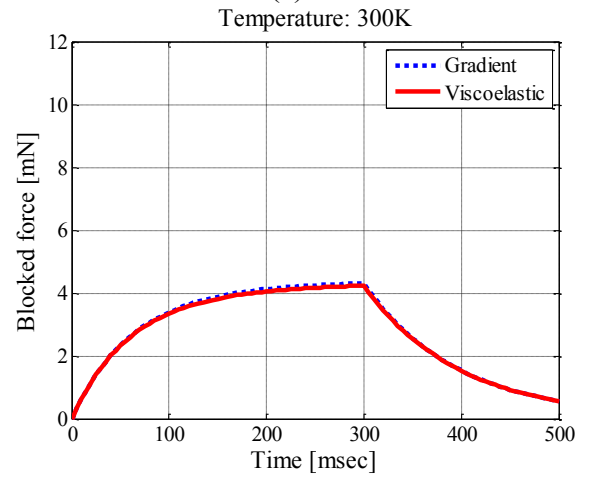
Figure 5.19. Blocked force comparison of gradient bending model and viscoelastic model: (a-c) varying Young's modulus and (d-f) constant Young's modulus

Chapter 6 : Conclusions and Future Work

6.1 Research Summary

The research in this dissertation focuses on the development of a smart material design, modeling and material selection tool. The polymers and smart materials software (PSMS) is developed in Microsoft$^®$ Visual Basic 2010. Comprehensive data on smart materials were collected and compiled into the material selection tool by conducting an extensive survey of published articles relevant to material properties, material-level models, system-level simulation models, and system-level smart material applications. This research focuses on a number of popular smart materials and material systems. Currently available mathematical models and potential applications were identified to select the best model for the tool. In areas where existing models were inadequate for system-level integration, new models were developed. Under this framework, this research seeks to develop a bending model of light-induced LCEs. As a result, the PSMS provides a wider variety of design and selection features for the users of polymers and smart materials.

In Chapter 2, the design of the software interface and material database is introduced. The software tool is constructed with three distinct interfaces: the material database interface; design & modeling interface, and performance data interface. The material databases include each material property and/or material type. The material databases, created using Visual Basic and MS Access™, also provide functions to add,

89

delete, edit, and select content depending on users' specific needs and purposes. Material systems and models are designed to provide material performance. The GUI-based computer software determines and simulates what material to use based on properties and performance. With regard to the polymers selection tool, polymer types and properties, polymeric behavior, and dielectric elastomers are discussed.

In Chapter 3, the "Smart Materials" tab and "Information" tab are discussed with primary emphasis on the smart materials tab. The "Smart Materials" tab is comprised of piezoelectric ceramics/polymers, shape memory alloys/polymers, thermoelectrics, and ER and MR fluids. According to their functionalities, they are categorized into four groups: actuators, sensors, energy generators, and passive structural materials. The diverse properties of the materials in each group are characterized and compiled into databases. In addition, reliable mathematical models for smart materials are coded into the software tool for various applications. At the end of chapter 3, the "Information" tab is discussed focusing on additional information such as external databases and cost.

In Chapter 4, the accuracy and the effectiveness of the smart materials selection tool are evaluated by comparing the tool's performance results with available experimental or simulation results from other published articles. The experimental verification of the material models shows the reliable performance of the selection tool. The examples that show how the software can be used to design smart material systems are provided in terms of dielectric elastomers, piezoelectric actuators, SMA wire application, and thermoelectric power generator application. In addition, material property and performance charts are provided for comparison of selected material types.

In Chapter 5, new models of light-induced LCEs are developed and a simplified bending model is incorporated into the tool. The gradient bending model, which is developed by Jin et al. [56], is discussed. The model considers the photo-isomerization process and the nematic-isotropic phase transition. However, the gradient bending model has difficulty in incorporating for system-based implementation because it is a time implicit model. Based on the gradient model, a simplified bending model is proposed to further develop a time-explicit viscoelastic photo-strain model. The simplified bending model is obtained by relocating the origin of a coordinate system and integrating the multiplication of strain and Young's modulus throughout an LCE film thickness. The viscoelastic photo-strain model, which is based on the Voigt-Kelvin model, considers photo-strain effect, temperature effect, and strain variation through an LCE film thickness.

6.2 Contributions

The chief contribution of this research is the development of a comprehensive and effective smart material selection tool, PSMS, which incorporates material properties, material-level models, system-level simulation models, and system-level smart material applications. Developing a comprehensive smart material selection tool significantly contributes to the future growth of the smart material field. In addition, this research developed new light-induced LCEs models: a simplified bending model and a viscoelastic photo-strain model. The time-explicit viscoelastic photo-strain model contributes to incorporating for system-based implementation.

The PSMS represents a technological advantage to the extent that it uses a much wider range of smart materials than any other smart material selection tool currently

available. The smart materials used include dielectric elastomers, liquid crystal elastomers, piezoelectric ceramics/polymers, shape memory alloys/polymers, thermoelectrics, and ER and MR fluids. Because this wide range of materials was investigated, extensive information about these materials and their properties are provided in the PSMS database, and this information is useful for material engineers in further applications of smart materials.

An important innovation in the PSMS is its corporation of mathematical models into a smart material selection tool. Furthermore, the tool interface was designed specifically for modeling performance based usage. This provides new options for users to develop their own smart material design and to enhance the accuracy of their decision making.

The PSMS employs a framework which provides a flexible user-defined environment. Users are capable of accessing the database in order to add new data, or modify existing data from a current version of the selection tool. Since the tool allows users to run material models from a variety of different material types and specifications, the software tool enables users to determine the best material for a smart material application and its performance criteria. The flexibility of the tool also allows it to be updated based on changes in software. Another feature of the PSMS is the ease of data transfer. It is a stand-alone selection tool which is an installable file system for Windows that pulls material data directly from Microsoft office databases with no intermediate steps.

6.3 Future Work

In the future, extensive data and available models for electrostrictive and magnetostrictive materials will be incorporated into the PSMS. The software will enable users to access the database in order to acquire more information such as reference, applications, and materials development relative to the manufacturability, repeatability, and durability. Experimental tests can be conducted to further verify the material models given on this smart material database.

References

[1]   BCC Research. *Smart Materials and Their Applications: Technologies and Global Markets*, Advanced Materials, Retrieved October 27, 2011 from www.bccresearch.com/report/smart-materials-technologies-markets-avm023d.html.

[2]   P.S. Ramalhete, A.M.R. Senos, C. Aguiar. Digital tools for material selection in product design. *Materials and Design*, 31:2275–2287, 2010.

[3]   MatWeb. Retrieved June 7, 2012 from www.matweb.com.

[4]   S.M. Sapuan. A knowledge-based system for materials selection in mechanical engineering design. *Materials and Design*, 22(8):687–695, Dec. 2001.

[5]   N.S. Ermolaeva, K.G. Kaveline, and J.L. Spoormaker. Materials selection combined with optimal structural design: concept and some results. *Materials & Design*, 23(5):459–470, Aug. 2002.

[6]   H. Breuer, M.H. Tiba, R. Shastri, S.J. Itkin, P.M. Sarnacke, R.A. Latham, W.B. Hoven-Nievelstein, K.S. Mehta, J.S. Kennedy, J.A. Grates, and G.P. Diehl. Global Standardization of the Acquisition and Presentation of Comparable Data on Plastics. *SAE Technical Paper 940438*, 103(5):237–242, 1994.

[7]   M.F. Ashby. *Materials selection in mechanical design*. Butterworth-Heinemann, Boston, 3rd edition, 2005.

[8]   X. Zha. A web-enabled open database system for design and manufacturing of micro-electro-mechanical systems (MEMS). *The International Journal of Advanced Manufacturing Technology*, 32(3):378–392, 2007.

[9]   Granta Design. *Granta's History*, Retrieved June 17, 2012 from www.grantadesign.com/company/history.htm.

[10]   Material ConneXion. History & Leadership, Retrieved July 3, 2012 from www.materialconnexion.com/Home/AboutUs/HistoryLeadership/tabid/104/Default.aspx.

[11]   P. Ramesh. *Smart materials for electromagnetic and optical applications*. Ph.D. dissertation, The Ohio State University, 2012.

[12] Y. Bar-Cohen. Electroactive Polymer (EAP) Actuators as Artificial Muscles—Reality, Potential and Challenges. *(Bellingham, WA: SPIE Optical Engineering Press)*, 2001.

[13] M. Wissler and E. Mazza. Modeling and simulation of dielectric elastomer actuators. *Smart Materials and Structures*, 14(6):1396–1402, Dec. 2005.

[14] R.E. Pelrine, R.D. Kornbluh, and J.P. Joseph. Electrostriction of polymer dielectrics with compliant electrodes as a means of actuation. *Sensors and Actuators A: Physical*, 64(1):77–85, Jan. 1998.

[15] R. Pelrine, R. Kornbluh, Q. Pei, S. Stanford, S. Oh, J. Eckerle, and K. Meijer. Dielectric elastomer artificial muscle actuators: Toward biomimetic motion. *in Proc. SPIE*, 4695:126–137, 2002.

[16] G. Kofod and P. Sommer-Larsen. Silicone dielectric elastomer actuators: Finite-elasticity model of actuation. *Sensors and Actuators A: Physical*, 122(2):273–283, 2005.

[17] G. Kofod. *Dielectric elastomer actuators*. Ph.D. dissertation, The Technical University of Denmark, 2001.

[18] M.C. Boyce and E.M. Arruda. Constitutive models of rubber elasticity: a review. *Ann Arbor*, 1001:48109, 2000.

[19] R.W. Ogden. Large deformation isotropic elasticity-on the correlation of theory and experiment for incompressible rubberlike solids. *Proceedings of the Royal Society of London. A. Mathematical and Physical Sciences*, 326(1567):565–584, 1972.

[20] C.O. Horgan and G. Saccomandi. Constitutive modelling of rubber-like and biological materials with limiting chain extensibility. *Mathematics and Mechanics of Solids*, 7(4):353–371, 2002.

[21] O.A. Shergold, N.A. Fleck, and D. Radford. The uniaxial stress versus strain response of pig skin and silicone rubber at low and high strain rates. *International Journal of Impact Engineering*, 32(9):1384–1402, 2006.

[22] X. Zhu, Q. Wang, and Z. Meng. A functionally gradient piezoelectric actuator prepared by powder metallurgical process in PNN-PZ-PT system. *Journal of Materials Science Letters*, 14(7):516–518, 1995.

[23] S. Zhou, C. Liang, and C. A. Rogers. Integration and design of piezoelectric patch actuators. *Journal of intelligent material systems and structures*, 6(1):125–133, 1995.

[24] Q.M. Zhang, H. Wang, and L.E. Cross. Piezoelectric tubes and tubular composites for actuator and sensor applications. *Journal of materials science*, 28(14):3962–3968, 1993.

[25] M. Mitrovic, G.P Carman, and F.K Straub. Response of piezoelectric stack actuators under combined electro-mechanical loading. *International journal of solids and structures*, 38(24):4357–4374, 2001.

[26] G.H. Haertling. Rainbow ceramics- a new type of ultra-high-displacement actuator. *American Ceramic Society Bulletin*, 73(1):93–96, 1994.

[27] R.F. Hellbaum, R.G. Bryant, and R.L. Fox. *Thin layer composite unimorph ferroelectric driver and sensor*. U.S. Patent 5,632,841, issued May 27, 1997.

[28] E.H. Anderson. *Piezoceramic induced strain actuation of one- and two-dimensional structures*. M.S. thesis, Massachusetts Institute of Technology, Dept. of Aeronautics and Astronautics, 1989.

[29] H. Kawai. The piezoelectricity of poly (vinylidene fluoride). *Japanese Journal of Applied Physics*, 8(7):975–976, 1969.

[30] W. Nitsche, P. Mirow, and T. Dörfler. Application of piezoelectric foils in experimental aerodynamics. *Instrumentation in Aerospace Simulation Facilities, 1989. ICIASF'89 Record., International Congress on*, 57–65, 1989.

[31] D.J. Spearritt and S.F. Asokanthan. Torsional vibration control of a flexible beam using laminated PVDF actuators. *Journal of sound and vibration*, 193(5):941–956, 1996.

[32] R.C. Zhou, L. Zhihong, D.Y. Xue, J.K. Huang, and M. Chuh. Suppression of nonlinear panel flutter with piezoelectric actuators using finite element method. *AIAA journal*, 33(6):1098–1105, 1995.

[33] Q. Zhang, P.A. Lewin, and P.E. Bloomfield. PVDF transducers-a performance comparison of single-layer and multilayer structures. *Ultrasonics, Ferroelectrics and Frequency Control, IEEE Transactions on*, 44(5):1148–1156, 1997.

[34] W. Nitsche, P. Mirow, and J. Szodruch. Piezo-electric foils as a means of sensing unsteady surface forces. *Experiments in fluids*, 7(2):111–118, 1989.

[35] L.C. Brinson and M.S. Huang. Simplifications and comparisons of shape memory alloy constitutive models. *Journal of Intelligent Material Systems and Structures(USA)*, 7(1):108–114, 1996.

[36] C.M. Wayman and T.W. Duerig. An introduction to martensite and shape memory. *Butterworth-Heinemann, Engineering Aspects of Shape Memory Alloys(UK),* 3–20, 1990.

[37] K. Tanaka. A thermomechanical sketch of shape memory effect: one-dimensional tensile behavior. *Res Mechanica*, 2(3):59–72, 1986.

[38] C. Liang and C.A. Rogers. One-dimensional thermomechanical constitutive relations for shape memory materials. *Journal of Intelligent Material Systems and Structures*, 1(2):207–234, 1990.

[39] L.C. Brinson. One-dimensional constitutive behavior of shape memory alloys: thermomechanical derivation with non-constant material functions and redefined martensite internal variable. *Journal of intelligent material systems and structures*, 4(2):229–242, 1993.

[40] K. Gall, M. Mikulas, N.A. Munshi, F. Beavers, and M. Tupper. Carbon fiber reinforced shape memory polymer composites. *Journal of intelligent material systems and structures*, 11(11):877–886, 2000.

[41] C. Thill, J. Etches, I. Bond, K. Potter, and P. Weaver. Morphing skins. *The Aeronautical Journal*, 112(1129):117–139, 2008.

[42] M.M. Keihl, R.S. Bortolin, B. Sanders, S. Joshi, and Z. Tidwell. Mechanical properties of shape memory polymers for morphing aircraft applications. *Proceedings of SPIE*, 5762:143–151, 2005.

[43] C. Liang, C.A. Rogers, and E. Malafeew. Investigation of shape memory polymers and their hybrid composites. *Journal of Intelligent Material Systems and Structures*, 8(4):380–386, 1997.

[44] C. Wood. Materials for thermoelectric energy conversion. *Reports on progress in physics*, 51:459–539, 1988.

[45] G. Chen, M.S. Dresselhaus, G. Dresselhaus, J.P. Fleurial, and T. Caillat. Recent developments in thermoelectric materials. *International Materials Reviews*, 48(1):45–66, 2003.

[46] M.R. Jolly, J.W. Bender, and J.D. Carlson. Properties and applications of commercial magnetorheological fluids. *Journal of Intelligent Material Systems and Structures*, 10(1):5–13, 1999.

[47] J.D. Carlson, D.M. Catanzarite, and K.A.S. Clair. Commercial magnetorheological fluid devices. *International Journal of Modern Physics B*, 10(23):2857–2866, 1996.

[48] Y. Yu, M. Nakano, A. Shishido, T. Shiono, and T. Ikeda. Effect of cross-linking density on photoinduced bending behavior of oriented liquid-crystalline network films containing azobenzene. *Chemistry of materials*, 16(9):1637–1643, 2004.

[49] H. Finkelmann, E. Nishikawa, G.G. Pereira, and M. Warner. A new opto-mechanical effect in solids. *Physical review letters*, 87(1):015501-1–015501-4, 2001.

[50] D.K. Shenoy, D.L. Thomsen III, A. Srinivasan, P. Keller, B.R. Ratna. Carbon coated liquid crystal elastomer film for artificial muscle applications. *Sensors and Actuators A: Physical*, 96(2):184–188, 2002.

[51] M.H. Li and P. Keller. Artificial muscles based on liquid crystal elastomers. *Philosophical Transactions of the Royal Society A: Mathematical, Physical and Engineering Sciences*, 364(1847):2763–2777, 2006.

[52] S. Courty, J. Mine, A.R. Tajbakhsh, and E.M. Terentjev. Nematic elastomers with aligned carbon nanotubes: New electromechanical actuators. *Europhysics Letters*, 64(5):654–660, 2003.

[53] M.H. Li, P. Keller, B. Li, X. Wang, and M. Brunet. Light-driven side-on nematic elastomer actuators. *Advanced Materials*, 15(7–8):569–572, 2003.

[54] M. Warner and L. Mahadevan. Photo-induced deformations of beams, plates and films. *Physical Review Letters*. 92(13):134302, 2004.

[55] D. Corbett and M. Warner. Changing liquid crystal elastomers ordering with light – a route to opto-mechanically responsive materials. Liquid Crystals, 36(10-11): 1263–1280, 2009.

[56] L. Jin, Y. Yan, and Y. Huo. A gradient model of light-induced bending in photochromic liquid crystal elastomer and its nonlinear behaviors. *International Journal of Non-Linear Mechanics*, 45(4):370-381, 2010.

[57] T. Ikeda, M. Nakano, Y. Yu, O. Tsutsumi, and A. Kanazawa. Anisotropic bending and unbending behavior of azobenzene liquid-crystalline gels by light exposure. *Advanced Materials*, 15(3):201–205, 2003.

[58] M. Camacho-Lopez, H. Finkelmann, P. Palffy-Muhoray, and M. Shelley. Fast liquid-crystal elastomer swims into the dark. *Nature materials*, 3(5):307–310, 2004.

[59] H. Tobushi, T. Hashimoto, S. Hayashi, and E. Yamada. Thermomechanical constitutive modeling in shape memory polymer of polyurethane series. *Journal of intelligent material systems and structures*, 8(8):711–718, 1997.

[60] F.J. Lockett. *Nonlinear viscoelastic solids*. Academic Press, London, 1972.

[61] H. Tobushi, K. Okumura, S. Hayashi, and N. Ito. Thermomechanical constitutive model of shape memory polymer. *Mechanics of materials*, 33(10):545–554, 2001.

[62] M.L. Williams, R.F. Landel, and J.D. Ferry. The temperature dependence of relaxation mechanisms in amorphous polymers and other glass-forming liquids. *Journal of the American Chemical Society*, 77(14):3701–3707, 1955.

[63] C.D. Near. Piezoelectric actuator technology. *Proceedings of SPIE*, 2717:246–258, 1996.

[64] A.D. Danak. *Optimization of harvested energy In piezoceramic shells*. M.S. thesis, The Ohio State University, 2003.

[65] J.E. Hubbard. *Smart skin sensor for real-time side impact detection and off-line diagnostics*. U.S. Patent 5,797,623, issued Aug. 25, 1998.

[66] K. Otsuka and X. Ren. Recent developments in the research of shape memory alloys. *Intermetallics*, 7(5):511–528, 1999.

[67] S. Seelecke and I. Müller. Shape memory alloy actuators in smart structures: Modeling and simulation. *Applied Mechanics Reviews*, 57(1):23–46, 2004.

[68] Z. Wang, X. Zu, X. Feng, and J. Dai. Effect of thermomechanical treatment on the two-way shape memory effect of NiTi alloy spring. *Materials Letters*, 54(1):55–61, 2002.

[69] F.L. Tan and S.C. Fok. Methodology on sizing and selecting thermoelectric cooler from different TEC manufacturers in cooling system design. *Energy conversion and management*, 49(6):1715–1723, 2008.

[70] X. Wang and F. Gordaninejad. Dynamic modeling of semi-active ER/MR fluid dampers. *Damping and Isolation, Proceedings of SPIE Conference on Smart Materials and Structures*, 4331:82–91, 2001.

[71] G.M. Kamath, M.K. Hurt, and N.M. Wereley. Analysis and testing of Bingham plastic behavior in semi-active electrorheological fluid dampers. *Smart Materials and Structures*, 5:576–590, 1996.

[72] Q. Wang, Q. Zhang, B. Xu, R. Liu, and L.E. Cross. Nonlinear piezoelectric behavior of ceramic bending mode actuators under strong electric fields. *Journal of Applied Physics*, 86(6):3352–3360, 1999.

[73] Sinocera. *Piezoceramics: Stack actuator (multilayer piezoceramic actuators)*, Retrieved December 9, 2011 from www.sinocera.net/en/piezo_stack.asp

[74]   CTS Electronic Components. *PZT5A & 5H Materials Technical Data (Typical Values)*, Retrieved July 9, 2012 from http://www.ctscorp.com/components/pzt/downloads/PZT_5Aand5H.pdf

[75]   G. Riva, G. Orjela, and M. Boiocchi. *Tire with zero-degree, metal reinforcing strap made of a shape-memory alloy*. U.S. Patent 6,401,779 B1, issued June 11, 2002.

[76]   M. Yaqub, T. Tang, R. Ghabra, and J. Nantz. *Thermoelectric tire pressure monitor sensor*. US Patent Application Publication, US 2005/0248447 A1, issued Nov. 10, 2005.

[77]   J. Park and G. Washington. Advanced development of a smart material design, modeling, and selection tool. *ASME Conference Proceedings*, 1(5217):675–684, 2011.